INVESTIGATION AND DOCUMENTATION OF PYROCUMULONIMBUS CLOUDS

by

Annastasia V. Sienko

A thesis submitted in partial fulfillment of

the requirements for the degree of

Masters of Science

(Atmospheric and Oceanic Sciences)

at the

UNIVERSITY OF WISCONSIN-MADISON

2017

Acknowledgements

I would like to thank Bryan Baum for giving me the opportunity to investigate these pyroCb events through funding and your guidance. I would like to thank my academic advisor Grant Petty. Also, a huge thank you to Elizabeth Weisz for helping me with libRadtran. Without this help I'm not sure how I would have figured out the radiative transfer model. Another thank you to Scott Bachmeier who helped with the pyroCb blog and getting me started into investigating these pyroCbs. Also, a thank you to Tom Rink who helped me with HIMAWARI-8 retrievals a provided me the files to do so. Last but certainly not least, thank you to my parents who have stood by me through my undergraduate and graduate career.

Abstract

Pyrocumulonimbus clouds (pyroCb) are deep convective events produced by intense wildfires that transport smoke plumes into the upper troposphere/lower stratosphere (UT/LS). Documentation of these pyroCb events has been provided by a blog (http://pyrocb.ssec.wisc.edu) since 2013. Over 100 pyroCb events have been documented with near-real-time imagery and products from MODerate resolution Imaging Spectroradiometer (MODIS), Atmospheric InfraRed Sounder (AIRS), Visible Infrared Imaging Radiometer Suite (VIIRS), Cross-track Infrared Sounder (CrIS), and geostationary sensors. From these documented cases we investigate different meteorological conditions conducive to the occurrence of a pyroCb event. To better characterize an atmosphere that is more favorable for pryoCb generation, we examine the behavior of the mid-level water vapor, upper-level divergence, and low-level humidity. Other features, such as the convective available potential energy (CAPE), seem to be ineffective in determining whether a pyroCb event will occur. However, this conclusion may reflect issues with the representativeness of available sounding datat. We also investigate the radiative characteristics of a pyroCb event in geostationary imagery. In particular, radiative transfer model (libRadtran) is used to simulate both pristine liquid water and ice cloud properties. Subsequently, the model is used to simulate the impact of smoke layer on the liquid/ice cloud properties. Comparisons are made between the radiative transfer simulations and a pyroCb event documented in geostationary data. With this research we are able to explore certain meteorological conditions that are conducive to pyroCb events, and how these events affect the radiative balanace.

Table of Contents

List of Figures

List of Tables

1 Introduction

Biomass-burning events remain close to the surface, generating extreme amounts of smoke that travels far from the source. Biomass burning events include wildfires and prescribed fires with reports of 30,000 – 40,000 wildfires occurring annually (Stocks et al. 2000). These events release heat energy that is then propagated by conduction, convection, and radiation (Ichoku 2008). Biomass-burning events are a global source of atmospheric aerosols, and are known for having a strong impact on cloud properties (IPCC 2007). Additionally, these events are significant due to the mass amount of aerosols contributing to the "global radiative balance through the scattering and absorption of solar radiation" (Ichoku 2008). Knowledge about biomass-burning events is "crucial for understanding the long range transport of particle and reactive gases that can substantially alter the radiation balance and chemistry of the atmosphere" (Guan et al. 2010). Research into biomass-burning events and their atmospheric effects has been extensive, and more knowledge about these events has come from the advances of satellite imagery. Satellite imagery has been essential for detecting these fires, seeing the progression of the smoke plumes, and for determining the smoke plume injection height (Guan et al. 2010). Imagery has been imperative to see the movement of aerosols from these events. For instance, imagery helps to monitor air-quality and land-use changes (Ichoku 2008).

On occasion these events can become explosive. For instance, a wildfire can produce a pyrocumulonimbus cloud (pyroCb), which can loft smoke high into the troposphere and even into the lower stratosphere (Fromm et al. 2010). PyroCbs are fire started

cumulonimbus clouds that do not occur for every wildfire. These pyroCbs events are a newly discovered occurrence explored within the last decade. Scientists like Mike Fromm, Rene Servranckx, and David Peterson have spearheaded research on these events.

General cumulus and cumulonimbus clouds have been researched for decades. Deep cumulus and cumulonimbus clouds arise in a deep conditionally unstable layer and the presence of large-scale convergence (Riehl 1950; Riehl and Malkus 1961; Kuo 1974). A conditionally unstable layer allows the cumulus clouds to reach the upper troposphere and lower stratosphere, while large-scale convergence is a trigger for conditional instability (Kuo 1974). The role of cumulus clouds is to transport heat and moisture upward (Riehl 1950). Under certain conditions cumulus clouds can form into cumulonimbus clouds that have rain, lightning, and even hail associated with them. In addition, cumulus clouds are optically thick and can change the radiative balance.

PyroCb and pyroCu clouds reflect the structure of a general cumulus clouds. Pyro-convection (pyroCu) is a cumulus cloud generated from a wildfire. PyroCu are sensitive to the heat flux of the fire and the sensible heat from the fire is an important role for dynamic development (Trentmann et al. 2006). The development of pyroCu depends on the relationship “amongst atmospheric stratification, ambient moisture, and fire fluxes of heat and moisture” (Potter 2005; Ludrer et al. 2006, 2009; Freitas et al. 2007; Lareau 2015). If a pyroCu releases significant moist instability aloft it will trigger deep convective clouds known as pyroCbs (Lareau 2015). PyroCb events are fire-triggered cumulinumbus clouds and are different from pyroCu events because of their intensity and large updraft velocities.

PyroCbs have updraft velocities greater than $10ms^{-1}$ at the cloud base (Trentmann et al. 2006).

Since pyroCb clouds are cumulonimbus clouds, pyroCbs are characterized as storm clouds (Fromm et al. 2005). The storm cloud structure of a pyroCb forms from the sensible heat from fire emissions, latent heat in the form of water vapor, and aerosol particles acting as cloud condensation nuclei (CCN, Trentmann et al. 2006). Trentmann et al. (2006) explored how CCN would affect the dynamic evolution of a pyroCb event. Earlier studies suggested that increased CCN from the fire would result in increased convection by increased condensation (Wang 2005). However, Trentman et al. (2006) proved the excess CCN produced from the fire had a negative effect on convection dynamics because they delay freezing of cloud droplets and thus the release of latent heat of freezing.

Furthermore, pyroCb events are important to study because they inject smoke and other biomass-burning emissions into the upper troposphere/lower stratosphere (UT/LS; Fromm et al. 2010), and like other thunderstorms, pyroCbs involve ice formation, precipitation, and lightning (Fromm et al. 2010, 2012). In rare cases, pyroCb events can become so severe they include hail and tornadoes (Rosenfeld 2006). These pyroCb events have only recently been investigated, so further research is needed to understand how they form and where they are likely to form. Additionally, since pyroCbs inject combustion emissions into the UT/LS it is useful to examine their radiative implications.

The purpose of this research is to explore what meteorological conditions are conducive to pyroCb events so as to better predict these pyroCb events. Furthermore, this research explores how increased aerosols in the UT/LS would affect the radiative balance.

Meteorological condition data were obtained using global forecasting system data and radisonde sounding data, while the effects on the radiative balance were explored using a radiative transfer model. Results from the radiative transfer model were compared to actual satellite retrievals. Overall, this research suggests that there are no specific meteorological condition conducive to every pyroCb, and the amount of smoke deposited in the UT/LS from a pyroCb event can not be determined.

1.1 Significance of pyroCb events

Since 2000, observations of smoke in the lower stratosphere have been documented and linked to pyroCb events (Fromm et al. 2010). In addition, pyroCb events tend to have greater longevity than regular convection. A study by Lindsey and Fromm (2008) indicated that anvils from regular convection last around 12 hours, while pyroCb anvils persist for 18 to 29 hours. From this information it has been surmised that smoke aerosols have a direct affect on the convection (Lindsey and Fromm 2008).

Lofted emissions from pyroCb events can result in inter-regional and intercontinental transport of emissions within just a few days (Al-Saadi et al. 2007). The spread of these aerosols and emissions far from the source region could produce some climate consequences (Fromm et al. 2010). Furthermore, smoke particles in the free troposphere are shown to interact with meteorological processes (Peterson et al. 2015; Wang et. al 2006, Wang et. al 2013). Biomass emissions (e.g. black carbon particles) can be deposited on ice sheets, indirectly affecting the radiation balance (e.g. albedo). This causes atmospheric warming and increased melting (Peterson et al. 2015, Randerson et al. 2006,

Kopacz et al. 2011). Knowledge on how the aerosols from pyroCbs affect the radiative balance is important for climate implications.

1.2 Goals of this study

The goal of this study was twofold. The first goal was to undertake an initial examination of the radiative effects due to the presence of absorbing smoke layer. Smoke is produced by fires and injected into the UT/LS by pyroCb events, so understanding their radiative effects is important. Extreme aerosol loading from fires can result in small ice particles, and an abundance of ice particles changes the radiative properties of a cloud (Lareau 2016). Additionally, smoke particles scatter and absorb so they have an effect on the Earth's radiation budget (Luderer et al. 2006). Changes in the radiative balance can affect variables such as surface temperature. This proves that understanding how a pyroCb affects the radiative balance is essential to understand climate changes such as surface temperature. To simulate this a radiative transfer model was used to place an smoke layer above a separate ice cloud. When pyroCb events occur their aerosols usually spread out as an aerosol layer. This layer is usually higher in the atmosphere, around 11 km, and may overlie other existing ice cloud layers. In this thesis, initial calculations of how an absorbing aerosol (smoke) layer alters the radiative balance over ice clouds are undertaken.

The next goal of this research was to build on Peterson et al. (2015) research into the meteorological condition conducive to pyroCb generation. The meteorological conditions investigated in that paper were upper level convergence, Haines Index, mid-level relative humidity (RH), and upper tropospheric lapse rate. Throughout that paper they investigated meteorological conditions for two pyroCb events that occurred in the so-called

Rim Fire in August 2013 in California. The same meteorological conditions are further studied in this thesis with a much larger database of pyroCb and non-pyroCb events. In Peterson et al. (2015) they only looked at two pyroCb cases, in this thesis we are looking at 41 pyroCb cases. For consistency between this research and Peterson et al. (2015), data were collected from radiosonde sounding profile and from GFS for each pyroCb and non-pyroCb event.

2 Background

The literature on pyroCb events has been relatively sparse, although interest has increased in recent years. These events have gained "research attention due to their affect on vertical smoke transport, atmospheric chemistry, and cloud microphysics"(Lareau 2016). Previously the convective columns of pyroCb events have been fairly well researched (Potter 2005; Trentmann et al. 2006; Luderer et al. 2006, 2009; Freitas et al. 2007). However, no studies have directly looked at the initiation of pyroCu/pyroCb events (Lareau 2015). Fromm et al. (2000) first investigated smoke reaching the stratosphere from boreal forest fires in Russia and Canada. They first realized smoke was being lofted to the stratosphere by looking at the Polar Ozone and Aerosol Measurement (POAM), Stratospheric Aerosol and Gas Experiment (SAGE), and lidar outputs. Fromm and Servranckx (2003) postulated that the smoke from these fires was being lofted to the stratosphere by supercell convection. They did a case study on the Chisholm Fire that occurred from 28-29 May 2001 in Alberta, Canada. In conclusion, they found that intense forest fires combined with convection result in substantial stratospheric aerosols.

In 2006, Fromm et al. coined the name pyrocumulonimbus (pyroCb) to explain the combination of intense boreal forest fires with convection. In Fromm et al. 2006, they investigated a pyroCb event in the Northwest Territories from 3-4 August 1998. In this research they used GOES imagery to identify the origin of the smoke plume, and POAM III and SAGE II to observe the aerosol profiles. They found that the pyroCb could have occurred due to a cold front moving through the area, creating an environment of upward vertical motion and reduced stability. Additionally, they found through GOES imagery that these

pyroCb events create an optically opaque smoke cloud near the UT/LS. Similar research done by Domoah et al. 2006 investigated meteorological conditions and the transport of emissions from severe forest fires in the summer of 2004. Domoah et al. 2006 found it difficult to differentiate between regular deep convection and pyro-convection. However, they did find that the brightness temperature above the fire reached -60^{o}C, and suggested that the fire might help to trigger strong convection.

Up until this point there had been a lot of research into past pyroCb events and investigating the meteorological conditions and transport of aerosols from these events. Luderer et al. (2006) modeled biomass smoke injections in a large forest fire. This study used the knowledge of how these events form to better model an ideal environment. Their research examined model sensitivities to water vapor and sensible heat fluxes. They understood that convection was sensitive to the heat flux from the fire, and water vapor was important for injection height. Additionally, they started with the knowledge that deep convection depends on temperature, humidity, and wind shear (Luderer et al. 2006). To model the pyroCb events they used a cold front for initiation. Overall, this study found that sensible heat was the main parameter influencing convection of these pyroCb events.

Other research included two papers investigating the Chisholm fire pyroCb by Rosenfeld et al. (2006) and Fromm et al.(2008). Rosenfeld et al. (2006) researched a new idea in the pyroCb field. They looked at the microphysics of the pyroCb cloud. They wanted to see how the large amount of CCN produced from a fire and the strong updraft of a pyroCb event would affect the microphysical structure of a pyroCb cloud. Rosenfeld et al. (2006) concluded that while there was a lot of positive lightning in a pyroCb cloud, there

was little precipitation associated with the event. They suggested that pyroCb clouds actually suppress precipitation compared to neighboring cumulonimbus clouds.

On the other hand, the Fromm et al. (2008) research of the Chisholm fire confirmed research previously done by Fromm et al. (2000, 2003). In this paper, Fromm et al. (2008) investigated the Chisholm fire using satellite data. They used satellite imagery to analyze constraints on plume height, thickness, and particle size. Additionally, they used ground-based measurements coupled with space-based measurements to observe the pyroconvection. Essentially, this paper provided insight into the how smoke is transported from a pyroCb event and how it can be detected from satellite imagery.

The next advances in research in this topic were described by Fromm et al.(2010). This paper thoroughly explained what pyroCb events were and investigated pyroCb events in the early summer (June and July) of 2002 with a total of 18 pyroCbs. They summarized their advances in their research of pyroCb events and how they were first detected. From this research, Fromm et al. (2010) found that pyroCb events typically occur in the western United States and Canada right before sunset around 18 UTC in North America. Additionally, these pyroCb events had minimum satellite infrared brightness temperatures lower than $-40^{o}C$.

Another area that had been previously researched was the effects of smoke from pyroCb events on the radiative balance. Gatebe et al. (2012) used a Monte Carlo radiative transfer simulation to look at the angular distribution in a pyroCu. They concluded that there was strong particle absorption in a pyroCu cloud. Additionally, Gatebe et al. (2012) speculated that there is a “smoke core” in these pyroCu clouds possibly allowing for a

pathway for fire emissions to reach the lower stratosphere. However, this theory has yet to be further researched.

While most of the research looked at the movement of aerosols, there began to be more research into the dynamics leading up to these pyroCb events. McRae et al. (2013) investigated pyroCb development in Australia, a geographic area that had not previously been featured much in pyroCb studies. McRae et al. (2013) looked at cases in recent years to understand meteorological conditions conducive to pyroCb events. In the cases they studied they found that rugged landscape, fire channeling, and foehn winds helped to produce pyroCbs. However, they advised that more case studies are needed to improve the understanding of which factors contribute to all pyroCb events.

Additional research into meteorological conditions was done by Peterson et al. (2015). They investigated the Rim Fire occurring in August 2013 in California (37.5 N 120.5 W). Their main goal was to understand how these pyroCb events formed. They thought that improved understanding of pyroCb events would improve “methodologies currently used for regional fire weather, air quality, and visibility forecasts” (Peterson et al. 2015). From the knowledge from this study, they concluded that looking at more pyroCb events to understand the meteorological conditions would be important.

One of the salient meteorological conditions of that study is relative humidity (RH). RH was explored because it has been suggested that entrainment of water vapor in midlevels could be a primary driver of pyroCb development (Trentmann et al. 2006). Trentmann et al. (2006) state that water vapor enhances the smoke transport beyond the tropopause level. Similar theories were suggested by Peterson et al. (2015). Their

investigation concluded that during the two pyroCb events from the Rim Fire the RH values exceeded 60 % in the 650-450 hPa layer. They noted that high relative humidity values in these levels were conducive to high-based thunderstorms. Overall, high mid-level relative humidity was identified as a condition favorable for the ability to produce a high cloud structure.

In addition, Convective Available Potential Energy (CAPE) was the main parameter used to characterize the buoyancy of these pyroCb events and was extracted from radiosonde soundings (Peterson et. al 2010; Wallmann et al. 2010). The theory was that CAPE would help force a regular wildfire to become a pyroCb event. CAPE is calculated by integrating vertically the local buoyancy of a parcel from the level of free convection (LFC) to the equilibrium level (EL). The larger the CAPE value the more instability that is in the atmosphere; the more instability, the greater the updraft velocity (Doswell III and Schultz 2006). Peterson et al. (2015) assumed that pyroCb events would have large values of CAPE because they would need greater updraft velocities. CAPE is conventionally found from radiosonde data, and soundings vary in distance, altitude, and time from the actual pyroCb event. From the investigation of the Rim Fire, CAPE varied with these pyroCb events and was little to none. Based on the cases explored by Peterson et al. (2015), CAPE may not be a meteorological condition conducive to pyroCb generation.

A third meteorological condition investigated by Peterson et al. (2015) was the Haines Index. The Haines Index is intended to indicate whether the atmosphere above a fire will contribute to the development of the fire. Haines Index measures the stability and dryness above a fire. The Haines Index specifically is computed from the temperature

difference between 700 and 850 hPa and the dewpoint depression at 850 hPa. The Haines Index values typically range from 2 to 6. The lower Haines Index indicates a moist stable layer, while a larger Haines Index (5 or 6) indicate a dry unstable lower atmosphere (Haines 1988). Peterson et al. (2015) theorized for a pyroCb event to occur there would need to be a dry, unstable lower troposphere. This is found when the Haines Index is high (Peterson et. al 2015). A high Haines Index does not conflict with the previous requirement of a high mid-level humidity. The dryer lower atmosphere is ideal for the fire intensity, while the high mid-level RH is important for a high cloud base. For the pyroCbs associated with the Rim Fire the Haines Indices were 5 or greater (Peterson et al. 2015).

Finally, the Peterson et. al (2015) paper explored the upper level dynamics associated with these pyroCb events. For a better development of a dry thunderstorm (for the Rim Fire in California), they found that there needs to be an elevated moist layer ,which corresponds to an upper-tropospheric lapse rate (UTLR, 500-300 hPa) of -7.5^{o}C km^{-1} or less. This is essential for a high cloud base. Additionally, rising motion is needed to force the convection for these pyroCb events, which is indicated by negative convergence at 250 hPa (Peterson et al. 2015; Wallmann et al. 2010; Nauslar et al. 2013). From the pyroCbs during the Rim Fire, the UTLRs were around -7.5^{o}C km^{-1}. Additionally, both pyroCbs were associated with negative convergence at 250 hPa (Peterson et al. 2015).

From the prior research that was done on the Rim Fire, a set of meteorological conditions were suggested that could be conducive to pyroCb generation. These include CAPE, Haines Index, mid-level relative humidity, UTLR, and upper level convergence. In this thesis, we examine the same criteria, but with the benefit of a much larger set of pyroCb

events. Additionally, non-pyroCb events were investigated to understand what conditions differed between pyroCb and non-pyroCb events.

3 Data

Throughout this research, different ground-based and satellite sensors were used to collect data used for the investigation of these pyroCb events including GOES-15, HIMAWARI-8, and MODIS Terra. These data were used to test hypotheses advanced by Fromm et al. (2010) and Peterson et al. (2015) regarding the conditions for pyroCb occurrence.

Geostationary satellite data were used most often to track the development of the pyroCbs. While polar-orbiting sensors were important to see the progression of aerosols from the pyroCbs, the overpass times are limited to early afternoon, and pyroCbs generally occur in late afternoon. Therefore polar satellites were not useful for observing the development of a pyroCb event. To see these events develop, geostationary satellite data were primarily used. The geostationary satellites used were GOES-15 and HIMAWARI-8. GOES-15 was used for pyroCb events in the western United States, Canada, and Alaska. On the other hand, HIMAWARI-8 was used for pyroCb events in Australia and Russia. A more through description of these satellites is found in the following sections.

These pyroCb cases were documented using the pyroCb blog (pyrocb.ssec.wisc.edu); non-pyroCb cases were found using the Incident Information System (inciweb.nwcg.gov). The Incident Information System provides information on fires throughout the United States and Alaska. This website provided data on the fire name, start date, location, and other factors.

For all cases, radiosonde sounding data were used to investigate the upper levels above a fire. Some features considered by sounding data were CAPE, Haines Index, UTLR, and mid-

level RH. Since these radiosonde soundings launch every 12 hours and sometimes are not near the site of the pyroCb they were not the most reliable data source.

In addition to radiosonde data, Global Forecast System (GFS) data were also used. GFS is a model produced by National Centers for Environmental Prediction (NCEP) to show an accurate picture of the weather conditions above the pyroCb (NOAA). GFS data supplemented for sounding data over the pyroCb. GFS data were plotted using GEMPAK and different python programs. A description of these programs and their uses is found later on. GFS data gave a better perspective of the meteorological conditions above a pyroCb and closer to the time that a pyroCb forms.

3.1 Satellite Data

Satellite imagery was used to determine the location of the wildfire and the minimum brightness temperature in the related plume. The wavelengths for each geostationary satellite are discussed further below. For a pyroCu event to be considered a pyroCb the minimum brightness temperature has to be –40^{o}C or colder (Fromm et al. 2010). This threshold distinguishes a high cloud top reaching the UT/LS. Fromm does not go into detail how this threshold was set, but it is presumably associated with the homogeneous nucleation temperature of cloud ice and thus the appearance of a cirriform anvil on a developing convection cloud. GOES-15 provided data over western North America, while HIMAWARI-8 and MTSAT-2 were used for pyroCb events over Russia and Australia.

These satellite images were projected using the Man computer Interactive Data Access System (McIDAS, Suomi et al. 1983). There are several versions of McIDAS, but for the purposes of this research McIDAS-X was used. McIDAS-X is used to visualize and

manipulate geophysical data from a range of formats (Suomi et al. 1983). This gives the ability to visually observe the development a pyroCb. Since the program is interactive, I decided what day, time, and location to project. These variables were determined by the location, day and start time of the pyroCb. Depending on the satellite I could plot images every 10 to 30 minutes. The newer satellite HIMAWARI-8 allowed images to be plotted every 10 minutes, while GOES-15 allowed for every 30 minutes. From each time step a frame was saved and later made into an animation. This was useful to see the progression of smoke after development, and to see the development of the pyroCb itself.

3.1.1 GOES-15

The Geostationary Operational Environmental Satellites (GOES) are a family of geostationary satellite at roughly 35786 km above the Earth (Hilgler and Schmit 2011). The GOES-West (GOES-15) imager has a 2-km resolution with a subsatellite point at 0^{o}N 135^{o}W over the equator; it takes data over the western coast of the United States and Canada. One of the goals of GOES-15 is to collect a nearly continuous scan of imagery for interesting weather cases (Hillger and Schmit 2011). The rapid scan utility was useful to see the development of the pyroCb events as they occurred. Table 1 (Hillger and Schmit 2011) shows the different imager bands with their respective wavelengths and meteorological objects. Visible imagery (imager band 1) showed the development of pyroCb events and provided imagery of the convection that was occurring. To detect the fire hotspot imager band 2 was used (Figure 1). The wavelengths within this imager band fall into the mid-IR region. From Wien's law the mid-IR response becomes stronger as the temperature of the blackbody increases (Pozo et. al 1997). Therefore the mid-IR wavelength was effective for

detecting fire hotspots. Figure 1 shows an example of a pyroCb in British Columbia on 25 May 2015. On the left is Band 1 and on the right is Band 2 with the pyroCb circled in red. This is just one scene from an animation loop of this pyroCb. Band 4, also located in an atmospheric window at 10.7 µm, provided the minimum cloud-top brightness temperatures (Figure 2). Figure 2 shows an example of Band 4 plotted for the same pyroCb in British Columbia. The pyroCb event is circled in magenta with the minimum brightness temperature around -55^{o}C. This imagery established that this is indeed a pyroCb event.

Table 1: GOES-15 Imager Bands

GOES Imager Band	Wavelength Range (µm)	Central Wavelength (µm)	Meteorological Objective
1	0.53 to 0.75	.63 (GOES-13/15)	Cloud properties and surface features during the day
2	3.8 to 4.0	3.9	Low cloud/fog and fire detection
3	5.8 to 7.3	6.48 (GOES-12/15)	Mid-to upper-level water vapor
4	10.2 to 11.2	10.7	Surface or cloud-top temperature
6	12.9 to 13.7	13.3 (GOES-12/15)	CO_2band: Cloud detection

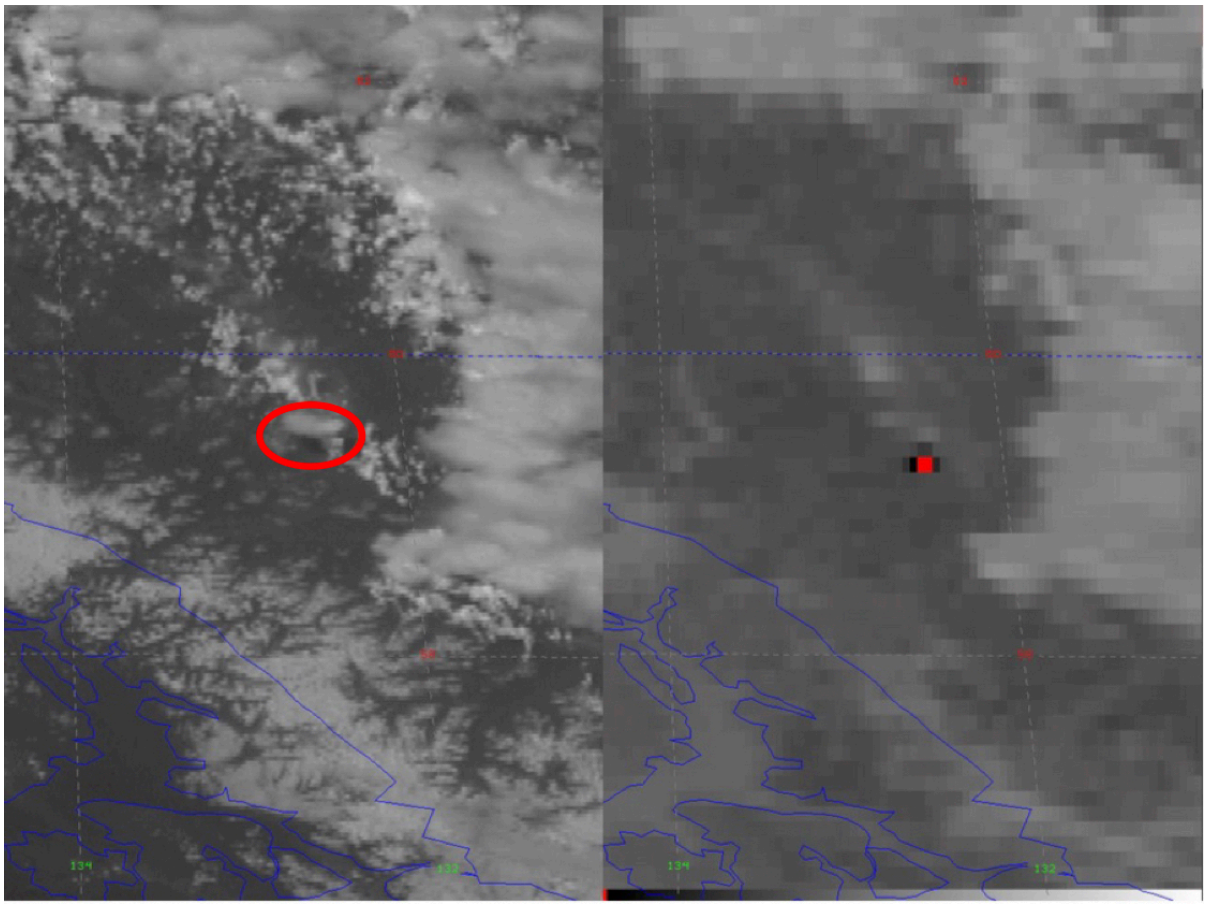

Figure 1. Example of pyroCb in British Columbia on 25 May 2015. Visible (0.65 µm) on the left and IR (3.9 µm) on the right. The pyroCb is circled in red.

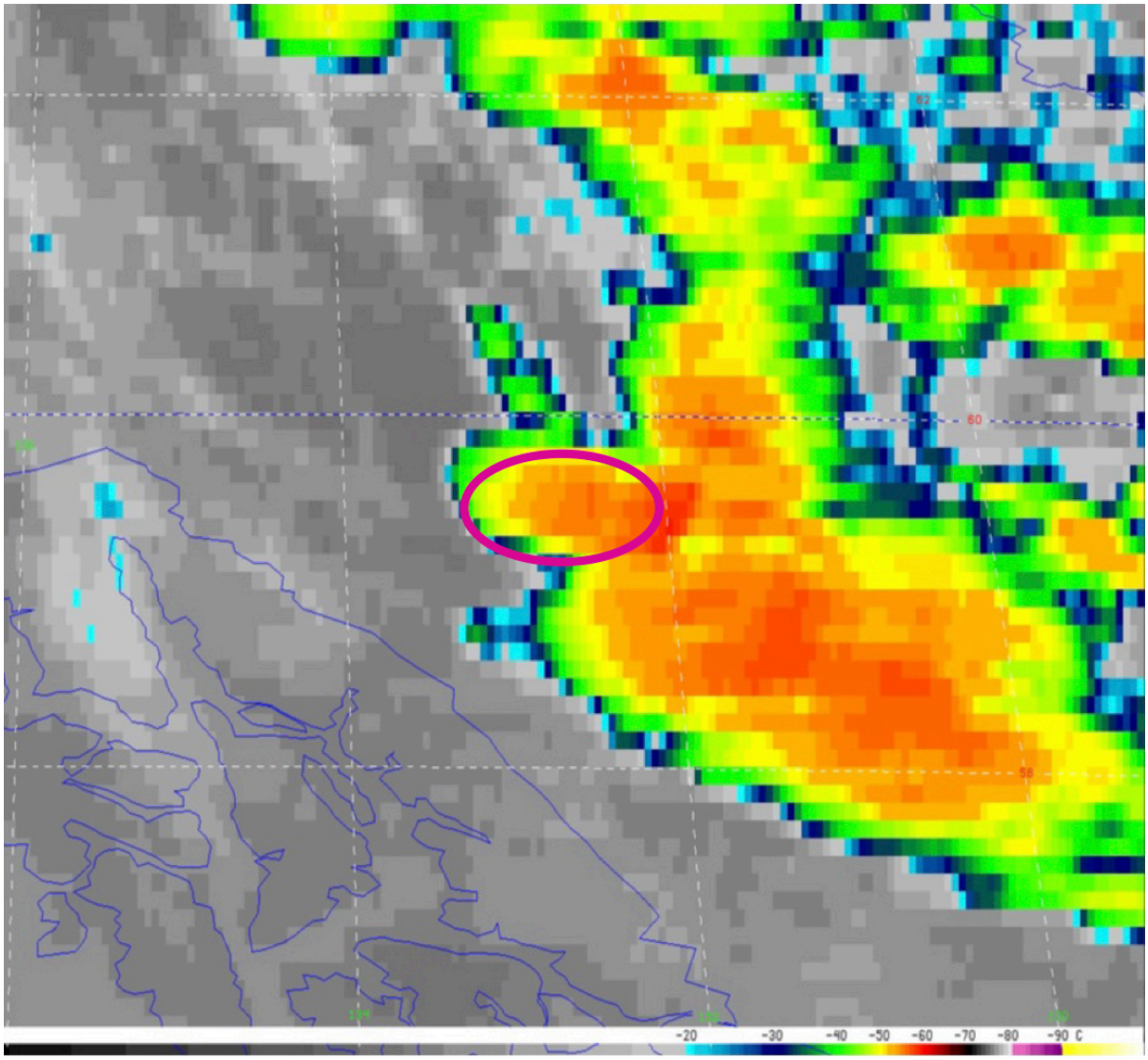

Figure 2. PyroCb event in British Columbia on 25 May 2015. The 10.7 µm brightness temperatures are shown. The pyroCb is circled in magenta.

3.1.2 HIMAWARI-8 and MTSAT-2

HIMAWARI-8 is a Japanese geostationary weather satellite launched by Japan Meteorological Agency (JMA). The satellite started its operational use on 07 July 2015 and replaced the Multifunctional Transport Satellite (MTSAT-2). This satellite provided imagery for pyroCb events in Russia and Australia. Before HIMAWARI-8 was in operation, the MTSAT-2, another JMA owned geostationary satellite, was used to track these pyroCb events in 2014 and most of 2015. Table 2 (Meteorological Satellite Center 2016) shows the central wavelengths for HIMAWARI-8 and MTSAT-2. The same features that were investigated with GOES-15 data were used with HIMAWARI-8 and MTSAT-2. Visible imagery (band number 4 or channel name VIS) was used to see the development of the pyroCb events. In addition, thermal IR (band 7 or channel name IR4) imagery was used to determine hotspots and the atmospheric window channel (band 13 or channel name IR1) was used to determine the coldest cloud-top brightness temperature. An example of this imagery is not shown, but similar imagery was produced like Figures 1 and 2.

Table 2: HIMAWARI-8 and MTSAT-2 Band Numbers

Band Number	Central Wavelength (µm,HIMAWARI-8)	Channel Name	Central Wavelength (µm, MTSAT-2)
3	0.63914	VIS	0.64
7	3.8853	IR4	3.9
8	6.2429	IR3	6.2
13	10.4073	IR1	10.4
15	12.3806	IR2	12.4

3.3 Non-pyroCb Cases

Not all wildfires produce a pyroCb event. The question was asked; what are the meteorological conditions that must be met for a pyroCb to form? To understand how these

pyroCb events occurred non-pyroCb ("null") cases were also investigated. These non-pyroCb cases were fires that occurred throughout the United States and Alaska that did not produce a pyroCb event. These non-pyroCb cases were important to interpret the difference between an environment that produced a pyroCb and one that did not. These non-pyroCb cases were found using the Incident Information System (inciweb.nwcg.gov). This site provided the name of the fire, start date, and position, which was helpful when documenting these non-pyroCb events and later investigate the meteorological conditions associated with each wildfire. This information was added to the pyroCb database and the meteorological conditions were analyzed the same as a pyroCb. The aim of this research was to measure the skill of a variable in distinguishing between pyroCb and non-pyroCb cases under otherwise similar circumstances. For this purpose, the Heidke Skill Score is employed; details are provided in section 4.2.6.

3.4 Weather Data

Radiosonde sounding data were used to investigate the atmosphere above a wildfire and were dependent on the location of the pyroCb and the time that it occurred. The sounding data were found using the University of Wyoming site (weather.uwyo.edu/upperair/sounding.html). The sounding data came in a variety of formats, but for the purposes of this research the text file format was used. The text file was essential for finding temperature, dewpoint, CAPE, and geopotential height values at certain levels in the atmosphere. The data were used to determine the relative humidity in the 450-650 hPa layer, the mid-level water vapor, and the amount of CAPE of a parcel originating from the surface. Additionally, the 300 and 500 hPa geopotential height and

temperature were used to calculate the lapse rate, and the 700 and 850 hPa temperature and 850 hPa dewpoint were used to calculate the Haines Index. Additionally, sounding data were used to complete an atmospheric profile for the radiative transfer equation. Note that sounding data is often unrepresentative due to the difference in time, distance, and elevation from the pyroCb. Due to these constraints radisonde sounding data were not ideal for determining local conditions affecting the pyroCb.

To mitigate the uncertainty of the sounding data, Global Forecast System (GFS) data were also used. The GFS data was plotted using a variety of data software tools, as further explained in the next sections. The GFS data were used to find the mid-level RH, Haines Index, UTLR, and divergence. CAPE was not found using GFS data due to programming limitations. These limitations were from the packages used to plot the variables. In both GEMPAK and python CAPE could not be plotted, so CAPE values were obtained solely from radiosonde sounding data.

3.5 Global Forecast System Analysis

GFS data were obtained from the Research Data Archive managed by the National Center for Atmospheric Research (NCAR). The files originally came from the National Center for Environmental Prediction (NCEP). These files were produced every six hours and were given at a variety of resolutions. These data from NCEP started archiving on 01 January 2011 and continues to present day. These data analyzes the products and forecasts of the atmospheric, oceanic and land surfaces (NCAR 2017). This data is very reliable with little to no data missing throughout this time frame.

For the purposes of this research files from NCAR were taken at times corresponding to the pyroCb event at 0.5 degree resolution and then plotted using the General Meteorology Package (GEMPAK). GEMPAK was created to analyze and display gridded meteorological data. GEMPAK was developed by NCEP to create an interactive user environment for research and education, but also to be used in operational forecasting. Plots were created to find values for the meteorological conditions near the fires location. The meteorological conditions that were investigated using GEMPAK were: 250 hPa convergence, the temperature at 700 and 850 hPa and the dewpoint at 850 hPa to calculate the Haines Index, the relative humidity in the 450- 650 layer to determine the mid-level water vapor, and the 300 and 500 hPa geopotential height and temperature to calculate the UTLR. These values were recorded for each case and then assessed for their conduciveness to pyroCb generation.

These GFS files were not only plotted using GEMPAK, but also using Python. The Python packages used were Windspharm and Cartopy. Windspharm is a Python package created by Andrew Dawson used to compute global wind fields in spherical geometry (Dawson). For the purposes of this research, this package was used to plot the 250 hPa divergence. The data found on UCAR website was converted into a NetCDF file. This netCDF file was then plotted using the Python package, and values of divergence could visibly be seen. An example of this can be seen in Figure 15. Furthermore, Cartopy is a Python package used to create maps to visualize data in an effective manner (Huner et al. 2002). Included in Cartopy is matplotlib, which is a Python 2D plotting library that generates plots, histograms, bar charts, etc (Hunter et al. 2002). The combination of these packages was

used to plot and analyze the meteorological conditions (e.g. relative humidity and temperature). This was efficient at determining values right above the pyroCb event.

4. Radiative Transfer Calculations

The first part of my research involved exploring the differences in geostationary satellite measurements between ice clouds and smoke residing over the ice clouds. Plumes from pyroCb events extend into the UT/LS where ice phase clouds are prevalent. The goal of the radiative transfer equations is to match model outputs to actual satellite data. This would provide an estimate for how much smoke is deposited in the UT/LS from a pyroCb event. The radiative transfer model wass run for one specific pyroCb event in eastern Australia. Since there is only one pyroCb event under investigation we cannot generalize and say that results will be the same for every pyroCb event. However, the goal for this research is to set a basis for further research into other pyroCb events.

To infer how a massive injection of smoke above an ice cloud affects the interpretation of satellite data, I performed a series of radiative transfer calculations in which a smoke layer was placed above an ice cloud. A description of the radiative transfer model is provided in the next section. The smoke and ice clouds are placed in separate layers, rather than mixed in a single layer. There is a growing body of research about stratospheric aerosol layers, with the research focusing on the chemical composition and size of the aerosols.

In this study, a radiative transfer model is employed to simulate values of reflectance and brightness temperature, and these are compared subsequently to

measurements from HIMAWARI-8 imagery of a pyroCb event. The data were extracted from the geostationary imagery using Hyper-spectral Data Viewer for Development of Research Applications (HYDRA; Rink et al. 2007). A further explanation of HYDRA, the scene chosen, and the results will be provided in section 4.4.

4.1 Solving the Radiative Transfer Equation

Both regions of pristine ice clouds (i.e., no smoke) and of pyroCb activity (i.e., smoke over ice cloud) were needed to compare measured to simulated reflectance and brightness temperature values. We performed a series of radiative transfer calculations for both scenarios in hopes of finding smoke concentration that matched a pyroCb event.

The radiative transfer calculations were performed using a software program called libRadtran (Mayer and Kylling 2005). Within libRadtran there are different methods for solving the radiative transfer equations. One option for solving the radiative transfer calculations was the discrete ordinates radiative transfer (DISORT; Stamnes et al. 1988) approach. DISORT is well documented and provides the necessary bulk scattering properties for various aerosol types, liquid water clouds, and ice clouds. For ice clouds, there are a number of different bulk scattering models from which to choose. In this case, the baum ice cloud model was chosen. One of the primary benefits to the DISORT formulation is that the user can simulate a multilayered atmosphere, e.g., multiple cloud layers, or a mixture of aerosol and cloud layers. DISORT is the radiative transfer equation solver, therefore, there was more information needed to actual solve the radiative transfer equation. The required inputs for libRadtran for radiances at a given wavelength include vertical profiles of

temperature, humidity, trace gases, location of clouds and/or aerosol in the atmospheric column, and cloud liquid water content. These inputs varied for each scenario, but are explained in detail in the following sections.

The DISORT model can be solved using a series of equations explained in paper by Stamnes et al. 1988. They started with the equation that describes monochromatic radiation at a frequency ν through a plane-parallel medium (Chandrasekhar 1960):

$$\mu \frac{du_\nu(\tau_\nu,\mu,\phi)}{d\tau} = I_\nu(\tau_\nu,\mu,\phi) - S_\nu(\tau_\nu,\mu,\phi) \qquad (1)$$

where $I_\nu(\tau_\nu,\mu,\phi)$ is the specific intensity along a direction μ,ϕ at an optical depth τ_ν measured perpendicular to the surface medium. S_ν is the source function give by the equation:

$$S_\nu(\tau_\nu,\mu,\phi) = \frac{\omega_\nu(\tau_\nu)}{4\pi}\int_0^{2\pi} d\phi' \int_{-1}^{1} d\mu' P_\nu(\tau_\nu,\mu,\phi;\mu',\phi')I_\nu(\tau_\nu,\mu,\phi) + Q_\nu(\tau_\nu,\mu,\phi) \quad (2)$$

where $\omega_\nu(\tau_\nu)$ is single-scattering albedo and $P_\nu(\tau_\nu,\mu,\phi;\mu',\phi')$ is the phase function. Furthermore, they explained that for thermal emission in local thermodynamic equilibrium (LTE), the source term Q_ν is:

$$Q_\nu^{(thermal)}(\tau_\nu) = [1-\omega_\nu(\tau_\nu)]B_\nu[T(\tau_\nu)] \quad (3)$$

where $B_\nu(T)$ is the Planck function at frequency ν and temperature T. If u_ν in equations (1) and (2) describes the diffuse radiation only, then the Q_ν term for a parallel beam incident in the direction μ_0,ϕ_0 on a nonemitting medium is given by the equation:

$$Q_\nu^{(beam)}(\tau_\nu,\mu,\phi) = \frac{\omega_\nu(\tau_\nu)I_0}{4\pi} P_\nu(\tau_\nu,\mu,\phi;-\mu_0,\phi_0)\exp(-\tau_\nu/\mu_0) \quad (4)$$

where $\mu_0 I_0$ is the incident flux. They took:

$$Q_\nu(\tau_\nu,\mu,\phi) = Q_\nu^{(thermal)}(\tau_\nu) + Q_\nu^{(beam)}(\tau_\nu,\mu,\phi) \quad (5)$$

They omitted the ν subscript and expanded the phase function $P(\tau, cos\theta)$ in a series of $2N$ Legendre polynomials and the intensity in a Fourier cosine series (Chandrasekhar 1960, Stamnes et al. 1988):

$$I(\tau, \mu, \phi) \sum_{m=0}^{2N-1} u^m(\tau, \mu) cosm(\phi_m - \phi) \qquad (6)$$

Equations 1 and 2 can be replaced by $2N$ independent equations to obtain:

$$\mu \frac{du^m(\tau,\mu)}{d\tau} = I^m(\tau, \mu) - \int_{-1}^{1} D^m(\tau, \mu, \mu') I^m(\tau, \mu') d\mu' - Q^m(\tau, \mu) \quad (7)$$

where m=0,1,2,….,2N-1. The discrete ordinate approximation of equation 7 becomes (Stamnes and Swanson 1981, Stamnes and Dale 1981):

$$\mu_i \frac{dI^m(\tau,\mu_i)}{d\tau} = I^m(\tau, \mu_i) - \sum_{j=-N}^{N} w_j D^m\big(\tau, \mu_i, \mu_j\big) I^m(\tau, \mu_i) - Q^m(\tau, \mu_i) \quad (8)$$

where $i = \pm 1, \ldots \pm N$, and μ_i and w_i are quadrature points and weights. Since the single-scattering albedo $\omega(\tau)$ and the phase function $P_\nu(\tau_\nu, \mu, \phi; \mu', \phi')$ are functions of τ then equation 8 constitutes a system of 2N coupled differential equation which no analytic solutions exist (Stamnes et al. 1988). To obtain analytic solutions the medium is assumed to have adjacent homogeneous layers, which the single-scattering albedo and the phase function are taken to be constant at each layer (Figure 3, Stamnes et al. 1988). The DISORT model was used to calculate the top-of-atmosphere (TOA) radiances for clear sky and cloud conditions for a given wavelength (Baum et al. 2000). The DISORT model used in this research (Figure 3) had equally spaced layers that were 1 km thick from the surface to 35 km. The fire in Fig. 3 represents a pyroCb event where smoke is deposited into the UT/LS. The figure displays the ice cloud between 11 and 12 km with the smoke layer just above the ice cloud between 13 and 15 km.

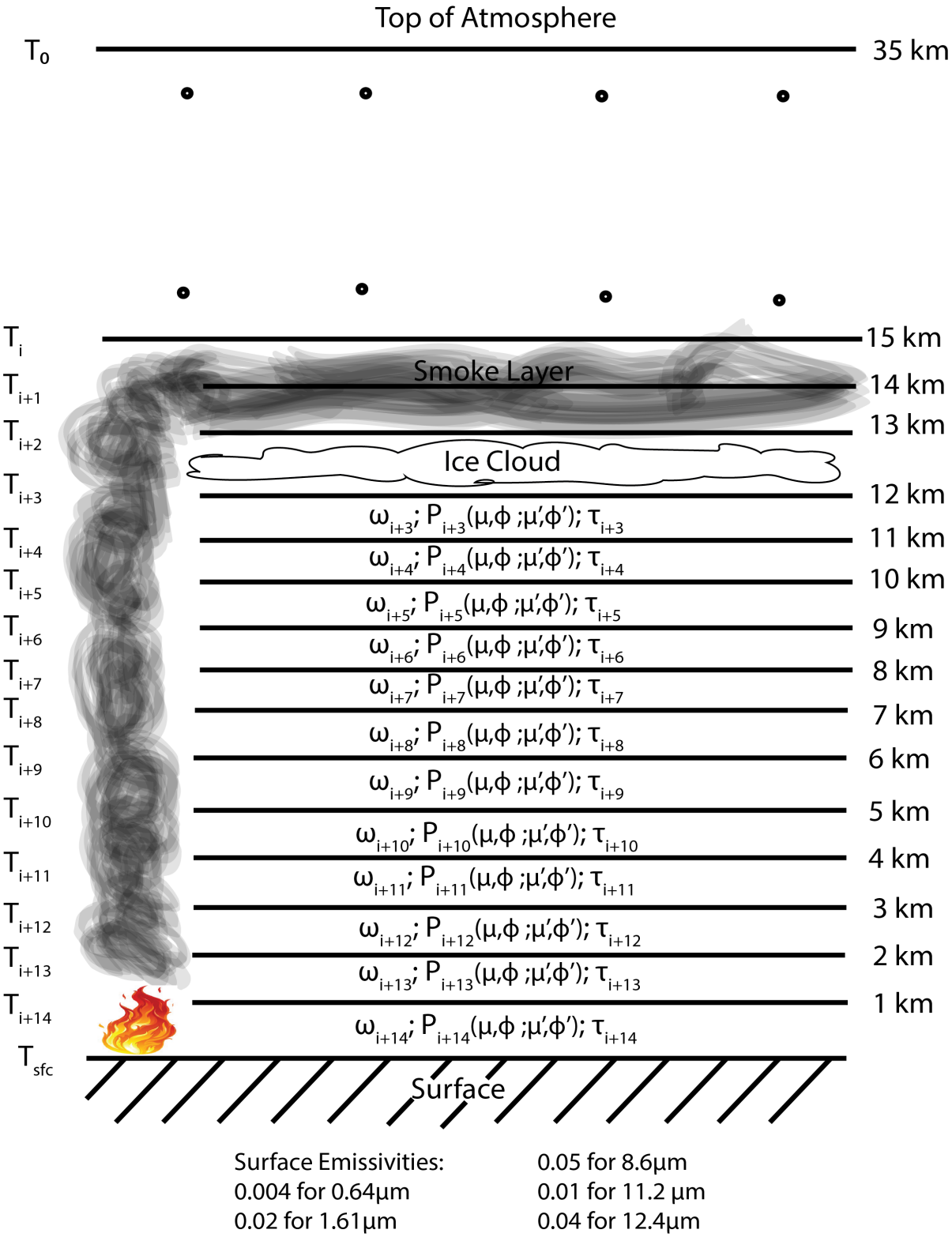

Figure 3. Model atmosphere used in discrete ordinates radiative transfer (DISORT) model. Each layer is characterized with a temperature (T), single scattering albedo (ω), phase function ($P(\mu, \phi; \mu', \phi')$), and optical thickness (τ). Additionally, the surface emissivities are labeled for each wavelength.

Libradtran was used to generate radiance simulations at both thermal and solar wavelengths. Three solar wavelengths (640, 1610, 2130 nm) and three thermal wavelengths (8.6 µm, 11.2µm, 12.4 µm) were selected, corresponding to central wavelengths for the channels on HIMAWARI-8.

The thermal wavelength radiances were converted to brightness temperature, while the solar wavelength radiances were converted to reflectances. The thermal and solar wavelengths chosen for detailed analysis were selected based on channels available on the geostationary imagers. For example, Baum et al. (2000) inferred cloud properties at thermal wavelengths such as 8.52 µm and 11 µm. The conversion from radiance to brightness temperature (T_B) was performed using the inverse of the Planck function:

$$T_B = \frac{hc}{\lambda k(\ln\left(\frac{2hc^2}{\lambda^5 I}\right)+1)} \qquad (9)$$

where h is the Planck's constant, c is the speed of light, k is Boltzmann's constant, λ is wavelength, T_B is brightness temperature, and I is radiance (Petty 2008).

Since pyroCbs occur over land, the RT calculations required surface albedo (for solar channels) and emissivity values (for infrared wavelength channels). Thermal wavelength surface emissivities were found using Combined ASTER and MODIS Emissivity for Land (CAMEL) compiled by the University of Wisconsin-Madison MODIS Infrared Emissivity dataset (UWIREMIS). The data can be found at NASA's website (https://lpdaac.usgs.gov/about/news_archive/release_nasa_measures_camel_5_km_products). The data provides monthly global data records for Emissivity, Uncertainty and Principal Component Analysis. The surface emissivities for the thermal wavelengths are found in

Figures 4-6. This data was taken for the pyroCb area a year prior to the pyroCb. From this dataset, it was found that the surface emissivity for 8.6 μm was 0.95, for 11.2 μm it was 0.99, and 12.4 μm it was 0.96. The surface emissivities are rough estimates from CAMEL data because the data are monthly averages from a year earlier.

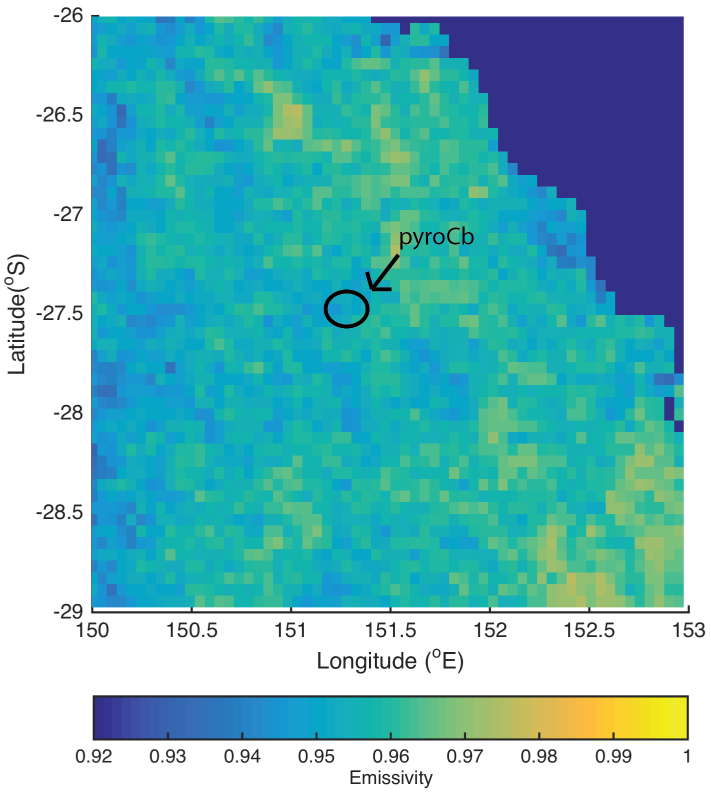

Figure 4. Surface emissivity at 8.6 µm from CAMEL averaged for the month of December 2015. This figure displays a pyroCb even on the eastern coast of Australia.

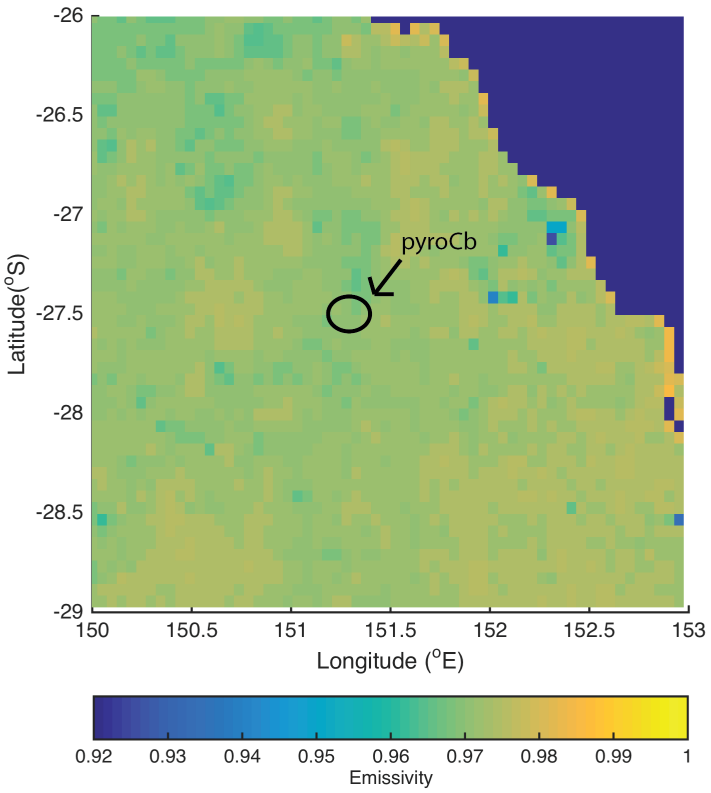

Figure 5. Surface emissivity at 11 µm from CAMEL averaged for the month of December 2015. This figure displays a pyroCb even on the eastern coast of Australia.

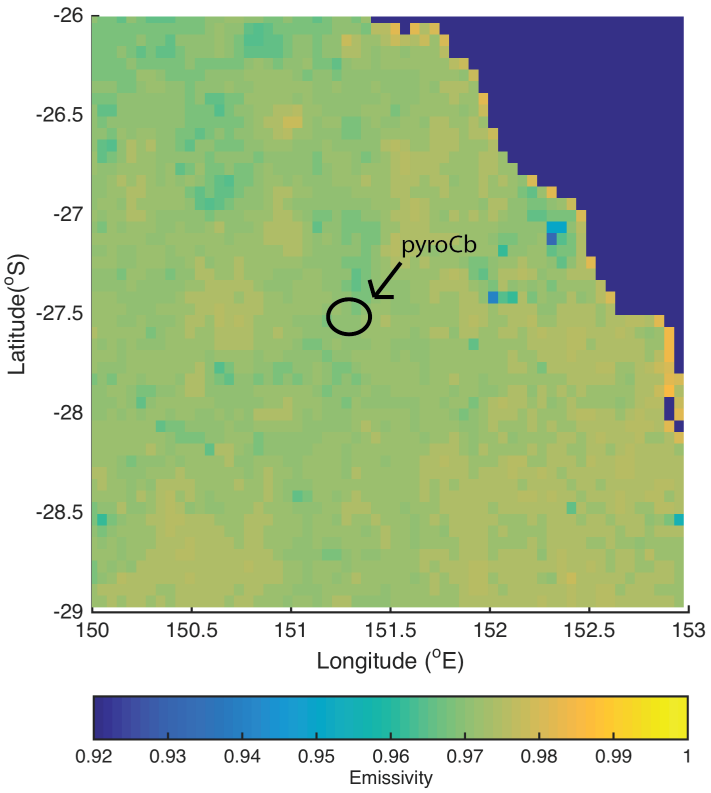

Figure 6. Surface emissivity at 12 µm from CAMEL averaged for the month of December 2015. This figure displays a pyroCb even on the eastern coast of Australia.

The solar wavelengths (640, 1610, 2130 nm) were used to investigate how reflectance varied with liquid water content as a function of particle effective radius. Reflectance was calculated using the equation:

$$reflectance = \frac{I\pi}{S_o \cos(\theta)} \qquad (10)$$

S_0 was dependent on the different wavelengths, while $cos(\theta)$ was constant with θ=67˚. This solar zenith angle was calculated for the geostationary data within Hydra from the time and location of the pyroCb event.

The HIMAWARI-8 reflectance data over the northwestern part of Australia were extracted for detailed analysis using HYDRA. The surface reflectance was found for the time of 4 December 2016 from 5-7 UTC due to a pyroCb event occurring at 6 UTC on this date. For the given date and area under investigation the average clear-sky surface albedos were 0.02 for 0.64 μm and 0.004 for 1.61 μm.

The model outputs from libRadtran for an aerosol layer above an ice cloud were compared to satellite measurements of an actual pyroCb event. HYDRA was used to view satellite images and determine the clear-sky radiances necessary for the radiative transfer simulations (Rink et al. 2007). HYDRA allows a user to move the cursor over an area for user-selected wavelengths, permitting close inspection of reflectances and brightness temperatures.

Another necessary input for the radiative transfer model was a representative atmospheric profile. This atmospheric profile provided the pressure, temperature, air density, water vapor, and other trace gases to better simulate the atmosphere in question.

The data for the atmospheric profile for this model simulation was from a radiosonde sounding near the pyroCb at 0 UTC on 04 December 2016. The radiosonde sounding profile provided pressure, temperature and relative humidity. Relative humidity had to be converted to mixing ratio for the radiative transfer simulations.

To convert relative humidity to mixing ratio, we followed this procedure. The number density of air was solved using the following equation (Jacob 1999):

$$n_a = \frac{P}{B_z T} \quad (11)$$

In the previous equation n_a is the number density of air (molecules per m^3), P is pressure (Pa), B_z is Boltzmann constant (1.38e-23$m^2 kgs^{-2} K^{-1}$), and T being temperature (K). The water vapor concentration was found using the number density of air and mixing ratio given in the sounding profile. The equation to find the water vapor concentration is given (Jacob 1999):

$$n_x = C_x n_a \quad (12)$$

In this equation, n_x is the water vapor concentration (molecules per m^3), C_x is the mixing ratio (kg/kg), and n_a is the number density of air (molecules per m^3). The other trace gases in the profile were inferred from the mid-latitude summer atmospheric profile given by libRadtran.

A skew-T plot of the atmospheric profile used is plotted below (Figure 7). Additionally, the ice cloud and smoke layer are indicated on the figure. Figure 7 demonstrates that there is some moistening in the mid-troposphere – this is a condition that has been observed with other pyroCb development (Peterson et al. 2015).

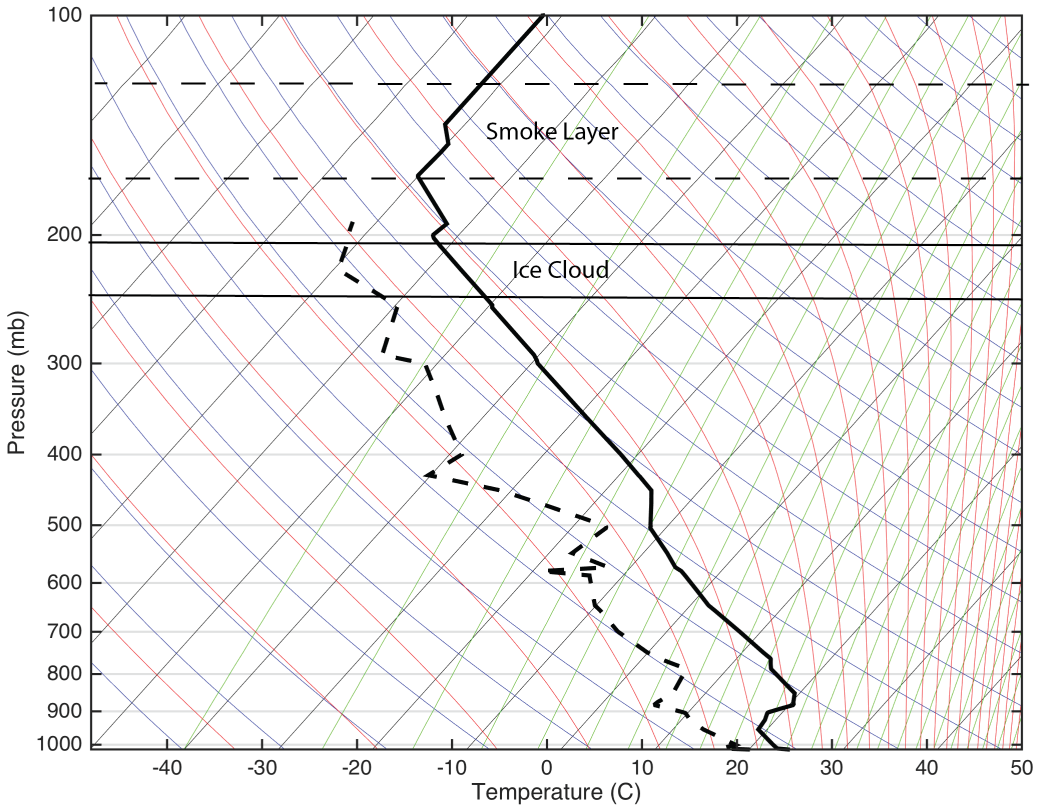

Figure 7. Skew-T diagram of sounding profile taken at Brisbane at 04 December 2016 at 0 UTC. This was used for the atmospheric profile provided to run the radiative transfer model for pristine ice cloud and smoke over pristine ice cloud.

4.2 Ice Clouds

Clouds in our atmosphere are composed of water, ice, or a combination of both. In water phase clouds, the water droplets are spherical. On the other hand, in ice phase clouds are a little more complicated compared to a water phase cloud due the complexity of the ice crystal shapes that form these ice clouds. In libRadtran, the difference between the ice and water clouds was that ice particles were non-spherical and liquid water particles are spherical (Mayer and Kylling 2005). The choice of the ice cloud bulk scattering models was dependent on the user's preference. For this research, the ice cloud bulk scattering model chosen was based on a "general habit mixture" named "baum" in libRadtran programming(Baum et al., 2014). The habit mixture employed severely roughened droxtals, hexagonal plates, hollow columns, solid columns, three-dimensional bullet rosettes, and multiple aggregates.

To provide insight into the behavior of ice phase clouds, four effective radii were chosen at 5, 10, 20, and 50 µm. The effective radius is the measure of the particle size used to calculate optical properties of clouds (Wyser 1998) .The effective radii are tied to the size distribution of these ice particles, and are based on the total particle volume divided by the total particle projected area for a given distribution of particles. For a distribution of spherical particles, the effective radius can be calculated by:

$$r_e = \frac{\int r^3 n(r) dr}{\int r^2 n(r) dr} \qquad (13)$$

where r_e is the effective radius, r is the particle radius (water droplets) and $n(r)$ is the number distribution with respect to r (Wyser 1998). For a nonspherical particle such as an

ice crystal the equation changes. For a nonspherical particle the size distribution is defined with respect to maximum length (L), where $n(L)dL$ is the number of ice particles per unit volume (Wyser 1998). Additionally, a better approximation for r is $r = 0.5(D^2L)^{1/3}$ Therefore, the effective radius is calculated by:

$$r_e = \frac{1}{2}\frac{\int D^2 L n(L) dL}{\int (D^2 L)^{2/3} n(L) dL} \qquad (14)$$

While it is important to understand how effective radii are calculated, these values were provided by the bulk scattering models within Libradtran.

The single scattering albedo ($\tilde{\omega}$) provides a measure of how much incident radiation at a given wavelength was scattered or absorbed in an ice cloud. The single scattering albedo ranged from zero in a purely absorbing medium to one in a purely scattering medium (Petty 2006). The single scattering albedo is calculated by the ratio of scattering and extinction cross sections:

$$\tilde{\omega}(\lambda) = \frac{\sigma_{scat}(\lambda)}{\sigma_{ext}(\lambda)} \qquad (15)$$

The scattering and extinction cross sections are defined as:

$$\sigma_{scat}(\lambda) = \frac{\int_{D_{min}}^{Dmax} [\sum_{h=1}^{M} \sigma_{sca,h}(D,\lambda) f_h(D)] n(D) dD}{\int_{D_{min}}^{Dmax} [\sum_{h=1}^{M} f_h(D)] n(D) dD} \qquad (16)$$

$$\sigma_{ext}(\lambda) = \frac{\int_{D_{min}}^{Dmax} [\sum_{h=1}^{M} \sigma_{ext,h}(D,\lambda) f_h(D)] n(D) dD}{\int_{D_{min}}^{Dmax} [\sum_{h=1}^{M} f_h(D)] n(D) dD} \qquad (17)$$

where λ is the specific wavelength, $\sigma_{sca,h}(D,\lambda)$ and $\sigma_{ext,h}(D,\lambda)$ are the scattering and extinction cross sections, M is number of habits, D is particle size, D_{min} is the minimum

particle size, D_{max} is the maximum particle size, and $n(D)$ is the particle density (Baum et al. 2014). These properties are provided by the bulk scattering ice model chosen in libRadtran.

Figure 8 displays single scattering albedo as a function of wavelength for an ice cloud. In this figure there are calculations based on four different effective diameters. This provided information about which wavelengths are more scattering as opposed to absorbing. For instance, for the visible channel (0.64 μm) the single scattering albedo is 1, indicating at this wavelength the pristine ice cloud is purely scattering. Additionally, at 1.61 μm, the single scattering albedos decrease, indicating that there is some particle absorption.

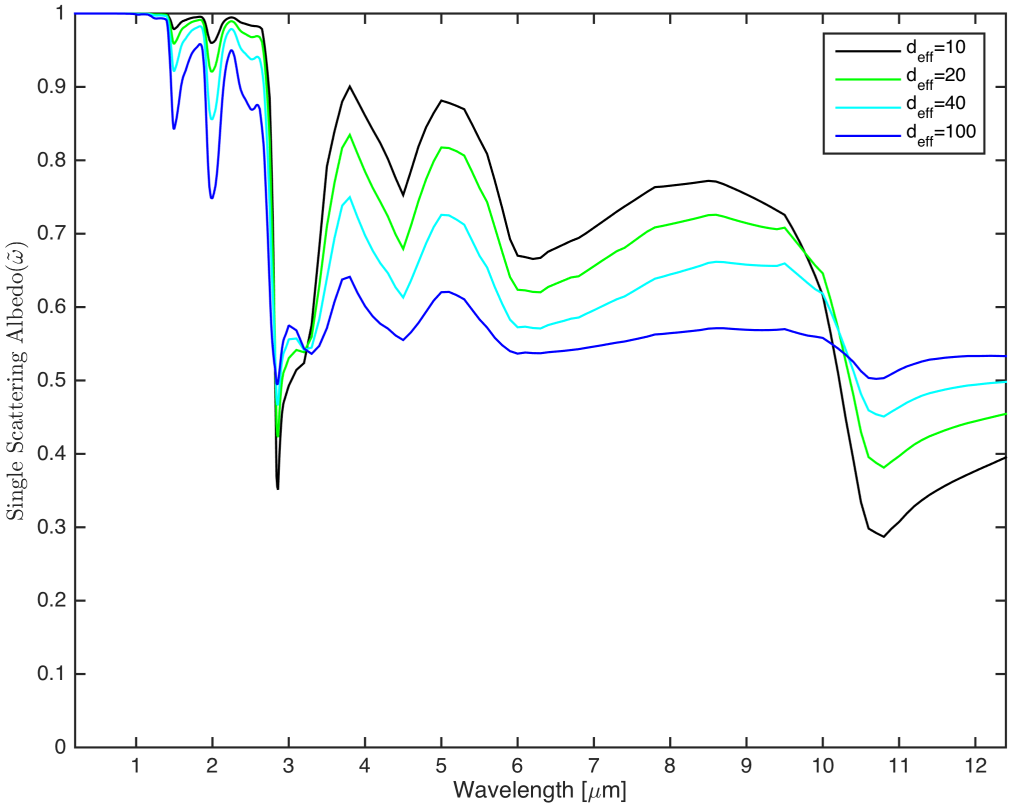

Figure 8. Single scattering albedo for a baum ice cloud as a function of wavelength (μm) with four different effective diamaters.

4.3 Smoke

Smoke changes the radiative effects of an atmosphere because smoke aerosols absorbs light across the shortwave region (Figure 9). As massive amounts of smoke are injected into the UT/LS during a pyroCb event, the optical thickness of the smoke layer increases. As the optical thickness increases the reflectance decreases due to increased absorption (Twomey 1977). In this scenario, this can affect the amount of solar radiation that penetrates the smoke layer. Our focus was limited to exploring how a smoke layer changes the top-of-atmosphere radiances (reflectances and brightness temperatures) over an ice cloud in Himawari-8 data for a pyroCb event. To explore how a pyroCb event may change the radiances emanating from an ice cloud, a smoke layer was placed above an ice cloud to simulate smoke injected into the UT/LS by a pyroCb event. This smoke layer was placed between 13 and 15 km, well above the ice cloud that was placed between 11 and 12 km.

In libRadtran there is a package called Optical Properties of Aerosol and Clouds (OPAC) that was used to determine the properties of smoke. There are not many options for aerosol selection in this program. Initially, the aerosol used was soot. Soot is composed of strongly absorbing black carbon molecules. Upon further examination it was decided that soot may not have the same properties of a biomass-burning event. The aerosol that best fit a biomass-burning event was the aerosol called water-soluble aerosol (WASO). This aerosol is used to describe anthropogenic aerosols, which include biomass-burning events (Hess et al. 1998). Within the package OPAC, Hess et al. 1998 calculated different optical properties

such as single scattering albedo. The mean single scattering albedo for a range of wavelengths was calculated using the following equation:

$$\overline{\omega}_0 = \frac{\int_{\lambda_{min}}^{\lambda_{max}} \omega_o(\lambda)\sigma_e(\lambda)E_o(\lambda)d\lambda}{\int_{\lambda_{min}}^{\lambda_{max}} \sigma_e(\lambda)E_o(\lambda)d\lambda} \qquad (18)$$

where E_o is the solar spectrum, σ_e is the extinction coefficient, and ω_o is the single scattering albedo at a given wavelength (Hess et al. 1998).

Figure 9 displays the single scattering albedo for WASO aerosol. One noticeable attribute is the single scattering albedo for WASO aerosol is less for solar wavelengths (0.64 and 1.61 μm) compared to the baum ice cloud (Fig. 8). This suggests that WASO aerosol absorb more at these wavelengths. On the other hand, the thermal wavelengths (8.6, 11.2, and 12.4 μm) have similar single scattering albedo values compared to the baum ice cloud. From this information, it is hypothesized that the brightness temperature values will have little change as the WASO aerosol layer's mass concentration is increased.

The WASO aerosol layer's mass concentration was changed to understand the impact of its presence for the six wavelengths described previously that match channels on Himawari-8. LibRadtran provides an aerosol profile for an urban atmosphere. The initial mass concentration of WASO aerosol at 13 km given in libRadtran was 1.484 e^{-7} g/m^3. The aerosol profile was modified by zeroing out the WASO concentration in each layer except for 13 to 15 km. I chose mass concentrations of $1e^{-4}$, $1e^{-5}$, and $1e^{-6}$ g/m^3 for the simulations, i.e., changing the WASO aerosol mass concentration in the layer by an order of magnitude, and compared the resulting radiances to Himawari-8 measurements. To find the total mass of WASO aerosols in the column the mass concentrations were multiplied by 2 km (2000 m).

This gave total mass concentrations of 0.2, 0.02, and 0.002 g/m^2. The results on which total mass concentration fit the HIMAWARI-8 data best are found in section 4.5.2.

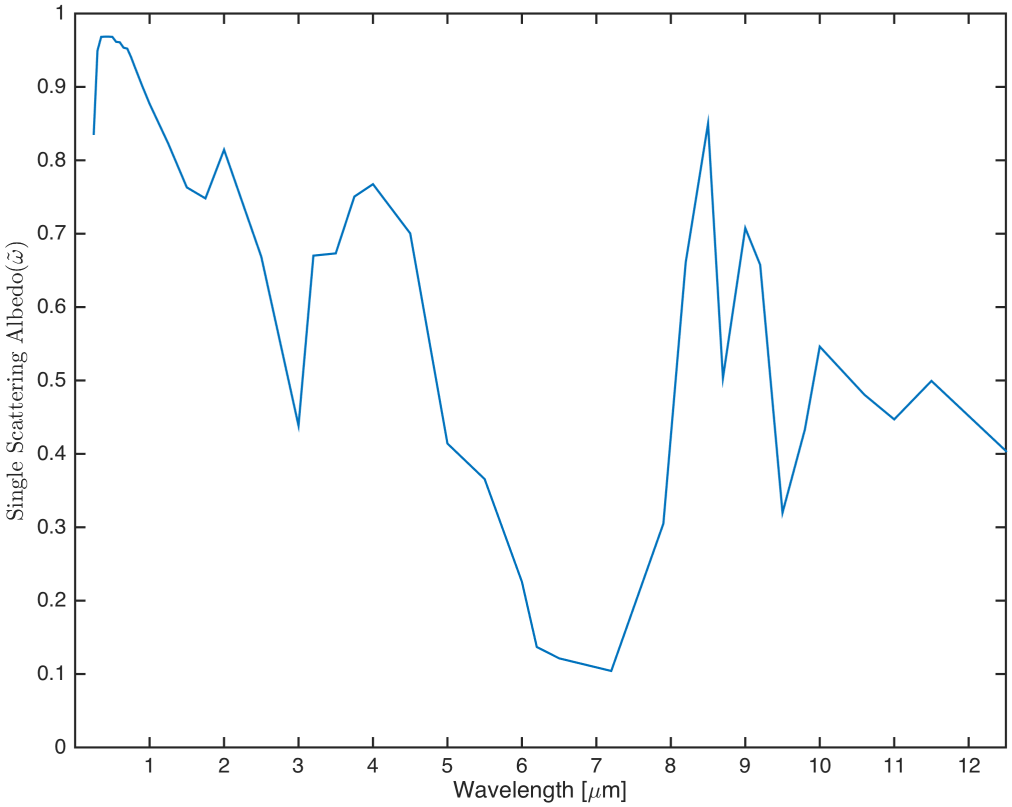

Figure 9. Single scattering albedo for water soluble aerosol as a function of wavelength.

4.4 HYDRA

Briefly described before, HYDRA is a software package that displays and analyzes remotely sensed multispectral and hyperspectral data (Rink et al. 2007). HYDRA was used to display HIMAWARI-8 imagery for solar and thermal wavelengths. For solar wavelengths, HYDRA displayed reflectance values, and for thermal wavelength HYDRA displayed brightness temperatures. Figure 10 shows an example of the 0.64 μm HIMAWARI-8 imagery at 06:30 UTC on 4 December 2016. The different boxes in this figure indicate areas where HIMAWARI-8 pixels were extracted for data points. The orange circle indicates the location of the pyroCb event. The turquoise box denotes the area where the smoke layer over ice cloud pixel data were extracted, and the purple box indicates the area where the pristine ice cloud pixel data were taken, in this case over water. The data from HYDRA were essential for understanding the difference between actual data and model simulations of a pristine ice cloud with a smoke layer above it.

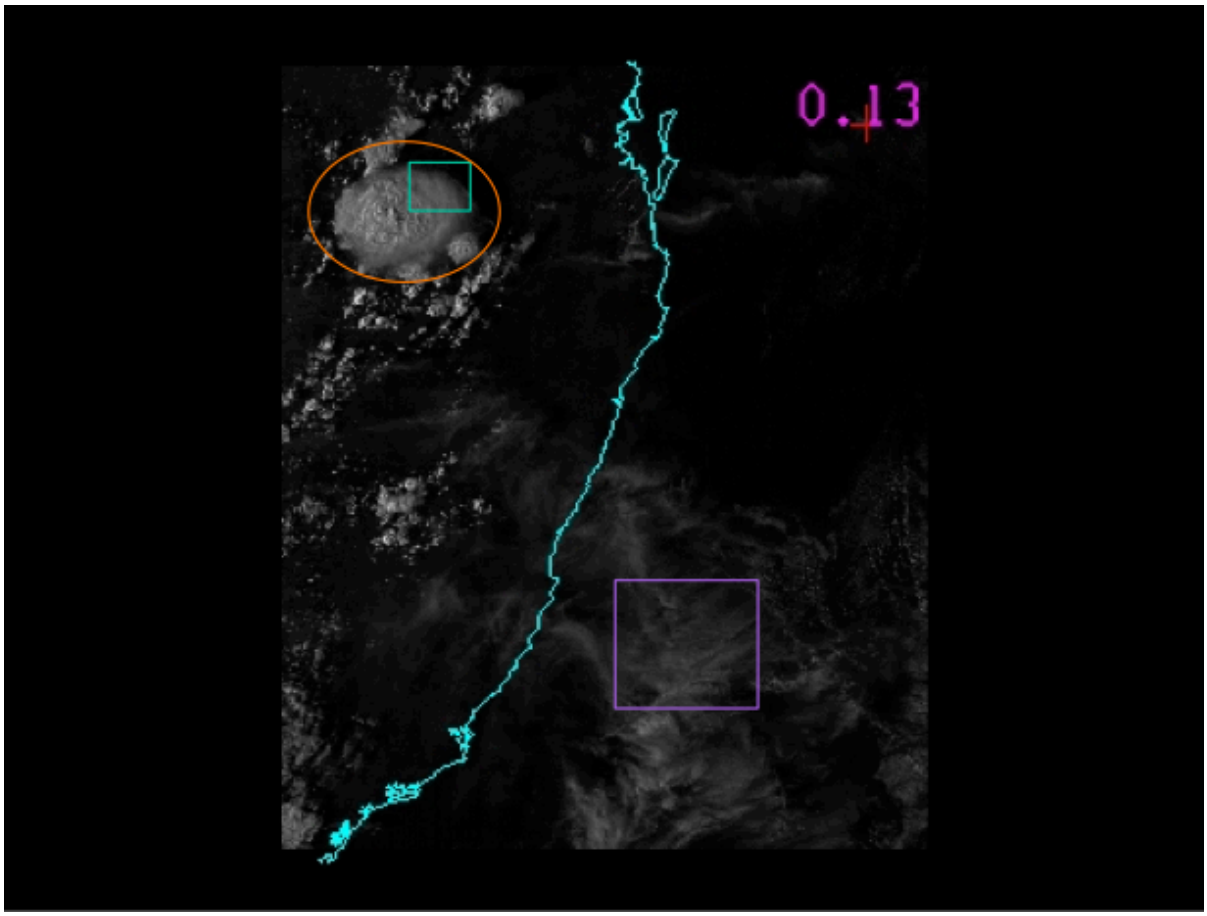

Figure 10. HYDRA scene at 0.64 µm of ice cloud and pyroCb event on the eastern coast of Australia taken on 4 December 2016 at 06:30 UTC . The orange circle is the pyroCb, turquoise square is the area of the pyroCb taken for data points, and purple square the ice cloud data points.

4.5 Results

The radiative transfer model was run for two scenarios. The first scenario was looking at an atmosphere with a pristine ice cloud over the ocean between 11 and 12 km with no aerosols. The second investigated an environment with a smoke layer residing between 13 and 15 km above an ice cloud. The ice cloud heights for both scenarios were decided based on the HYDRA data from this specific date and area. The results of these models are further explored below, and provided a basis when comparing to satellite data.

4.5.1 Pristine Ice Cloud Analysis

The area of the pristine ice cloud is displayed in Figure 10. This was the best example of a pristine ice cloud for the date and time in the vicinity of an active pyroCb. The ice cloud was over the ocean so changes had to be made to the model to account for this. The ice cloud height was determined by running the radiative transfer model several times (not shown) to match the model output to the HIMAWARI-8 data. Once the height of the cloud was determined small changes were made to fit the model data better to the actual data. For instance, since this ice cloud was over the ocean the water vapor profile was increased at lower levels. Additionally, the surface albedo was close to zero for all wavelengths, and the surface temperature was decreased from the land temperature. The ocean sea surface temperature was estimated from the brightness temperature at 11.2 μm. The brightness temperature at this wavelength was found to be 298.8 K. This temperature was use for all wavelengths because the surface brightness temperature did not vary by much for the

other thermal wavelengths, and this temperature was good estimate for the solar wavelengths.

The results from this model for a pristine ice cloud are shown in Figure 11 with the optical thicknesses labeled. From the radiative transfer model, the 11.2 µm brightness temperature ranged from about 214-294 K. This temperature range allowed for both ice cloud with different optical thicknesses and clear sky to be investigated.

The top two plots (Figure 11 a and b) are the reflectance versus the 11.2 µm brightness temperature with HIMAWARI-8 data superimposed in light blue. Two solar wavelengths were chosen based on the Himawari-8 visible (VIS; 0.64 µm) and shortwave infrared (SWIR; 1.61 µm) wavelengths. At lower optical thicknesses, approaching clear sky conditions, we observe the highest brightness temperature and the lowest reflectance values. For these calculations, optical thicknesses are based on the VIS channel, i.e., at 0.64 µm. As the optical thickness increased, the reflectances increased and the 11.2-µm brightness temperatures decreased (Figure 11 a and b). As the optical thickness increases, the reflectances increase monotonically, with the highest values tending to occur with the lowest effective diameter ice models. As the effective radius increases, the reflectance values tend to decrease. At 1.61 µm, the larger particle models tend to absorb more incoming radiation (lower single scattering albedo) relative to a wavelength such as 0.64 µm, for which scattering is conservative. The VIS channel can be used to infer optical thickness, while the 1.61-µm reflectances tend to have a larger sensitivity to effective radius (Nakajima and King 1990).

As the ice cloud becomes opaque, i.e., high optical thickness values, we note that the brightness temperature approaches the temperature of the cloud layer. Additionally, Figs. 11a,b indicate that the pristine ice cloud has a large optical thickness range with some pixels indicating an optical thickness greater than 20.

The next two plots (Figs. 11 c, d) depict how the brightness temperature differences change with brightness temperature at 11.2 μm. The brightness temperature differences (BTD) were calculated for BTD[8.6-11.2 μm] and BTD[11.2-12.4 μm]. Previous research has been done to infer ice cloud properties by looking at various BTDs (e.g., Stone et al. 1990; Baum et al. 1994; Baum et al. 2000). The BTD[8.6-11.2] values have greater sensitivity to effective radius than the BTD[11.2-12.4]. Both the BTD[8.6-11.2] and BTD[11.2-12.4] peak near an optical thickness of 3. The range of sensitivity to optical thickness is less than for solar channels. However, these BTDs provide complementary information to solar channel methods for optically thin ice clouds and have the additional benefit of being insensitive to the solar illumination. This can be useful for analysis of pyroCbs because these events tend to occur late in the day when the sun is low in the sky.

Notably different than the reflectance versus brightness temperature plots, the BTD plots would seem to indicate that the HIMAWARI-8 data are dominated by larger ice particles, rather than smaller particle models as indicated in Fig. 11b based on the 1.61-μm channel. This proves that while this radiative transfer model is useful for understanding the reflectance and brightness temperature values associated with a pristine ice cloud, it is not perfect. The model is a rough estimate of the atmosphere used and the ice cloud under investigation.

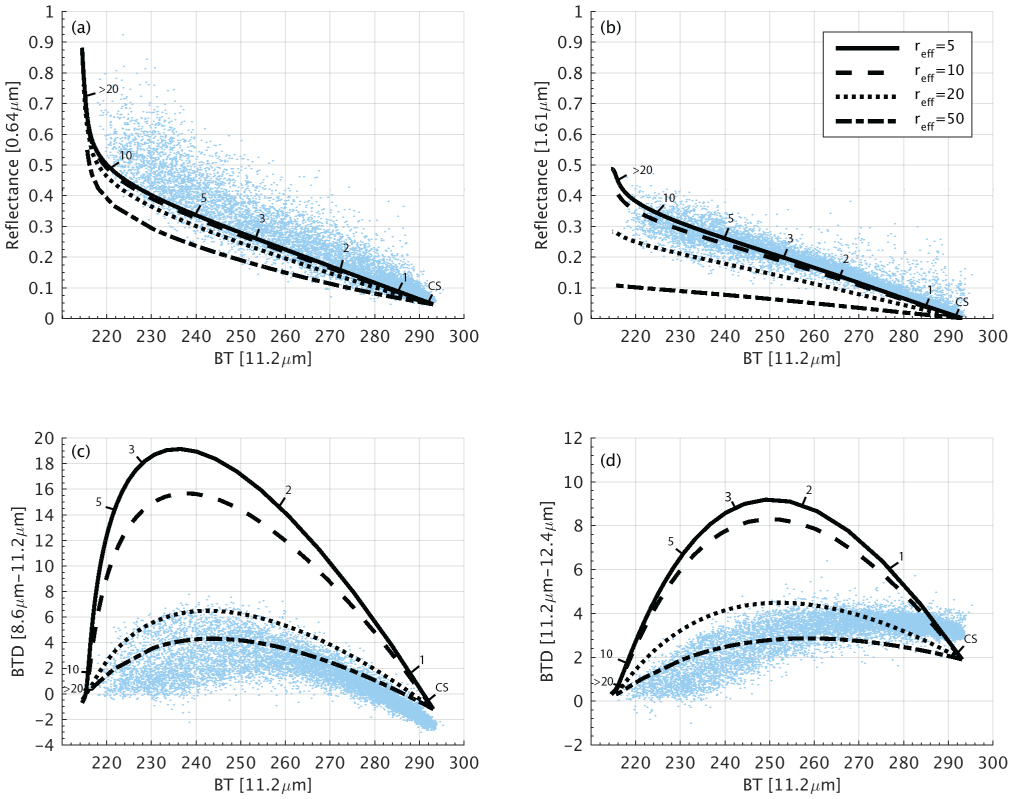

Figure 11. Radiative transfer model results for cloud composed of ice particles for (a) the reflectance at 0.64 µm versus the 11.2 µm brightness temperature, (b) the reflectance at 1.61 µm versus the 11.2 µm brightness temperature, (c) BTD (8.6 µm-11.2µm) versus the 11.2 µm brightness temperature, and (d) BTD (11.2 µm-12.4 µm) versus the 11.2 µm brightness temperature. Optical thickness and clear sky are labeled with HIMAWARI-8 data superimposed in light blue.

4.5.2 Analysis of smoke layer over an ice cloud layer

The next scenario in the radiative transfer equations was looking at an ice cloud with a smoke layer above it. This was explored to better understand the pyroCb data from HIMAWARI-8. For this set of calculations, the ice cloud was at the previous height with a WASO aerosol layer placed between 13 and 15 km. The atmospheric profiles are derived from the radiosonde profile used earlier. Additionally, surface albedo/emissivity were considered for all wavelengths, and the surface temperature was increased to 300 K. The surface temperature was found by looking at the 11.2 μm brightness temperature near the location of the pyroCb. An explanation of how the surface albedo/emissivity values were determined is found in section 4.1.

Figure 12 shows an ice cloud over land with varying WASO aerosol total mass concentrations above the ice cloud. The pyroCb data from HIMAWARI-8 is superimposed as blue scatter points on these plots. This figure shows results for a fixed value of effective radius of 20 μm with the optical thicknesses the same as the pristine ice cloud (not shown in figure). The HIMAWARI-8 BT[11.2 μm] data from the pyroCb range in temperature from 208 to 298 K. This suggests that the pyroCb event extended higher than the pristine ice cloud analyzed in the previous section. In addition, the warmer end of the BT range increased because the surface temperature was much higher over land than for the ice cloud analyzed over ocean.

As before, the first two panels (Figure 12 a and b) in this figure are reflectance versus BT, and the other two panels (Figure 12 c and d) are BTD versus BT. These panels provided insight into how WASO aerosol total mass concentration impacted the RT

calculations. Firstly, the model data from the ice cloud nor the aerosol layer model reach the lowest brightness temperatures retrieved from HIMAWARI-8 data. This suggests that either the ice cloud or the aerosol layer was higher in the atmosphere.

Additionally, near clear sky the VIS reflectance increased as the WASO total mass concentration increased (Figure 12 a). This is contrary to the previous belief that with more aerosols the solar channels will absorb more, thus reducing the reflectance values. Additionally, for both VIS and 1.61 μm there is no total mass concentration that fits the HIMAWARI-8 data best. The two WASO total mass concentrations that fit the data the closest were 0.02 and 0.002 g m^{-2}. From solely looking at reflectance values this proposes that the pyroCb event under investigation has a small WASO aerosol mass concentration.

The next two plots (Figure 12 c and d) of BTD versus BT show that the mass concentration has little effect on the BTDs. The one total mass concentration that seemed to change the most was 0.2 g m^{-2}. Near clear sky the BTD [8.6-11.2 μm] decreased for this mass concentration (Figure 12 c), but the BTD [11.2-12.4 μm] increased near clear sky (Figure 12d). This indicates that near clear sky the 11.2 μm brightness temperature increases with increased WASO total mass concentration. Note at clear sky for BTD [11.2-12.4 μm] the model data for 0.2 total mass concentration matches the model data perfectly. Other than this slight change near clear sky, the other total mass concentrations do not seem to vary from each other. They only slightly vary from the pristine ice cloud with the biggest differences near clear sky (Figure 12 c and d).

Overall, the model outputs provide little knowledge into the total mass concentration of aerosols in a pyroCb event. As mentioned earlier, these are the model

results for one case, so to generalize for all pyroCb events more cases are needed. From this single case it showed that matching model data to actual satellite retrievals is not by any means perfect. Furthermore, it proved that the exact total WASO aerosol mass concentration is difficult to find for a pyroCb event, and is still unknown.

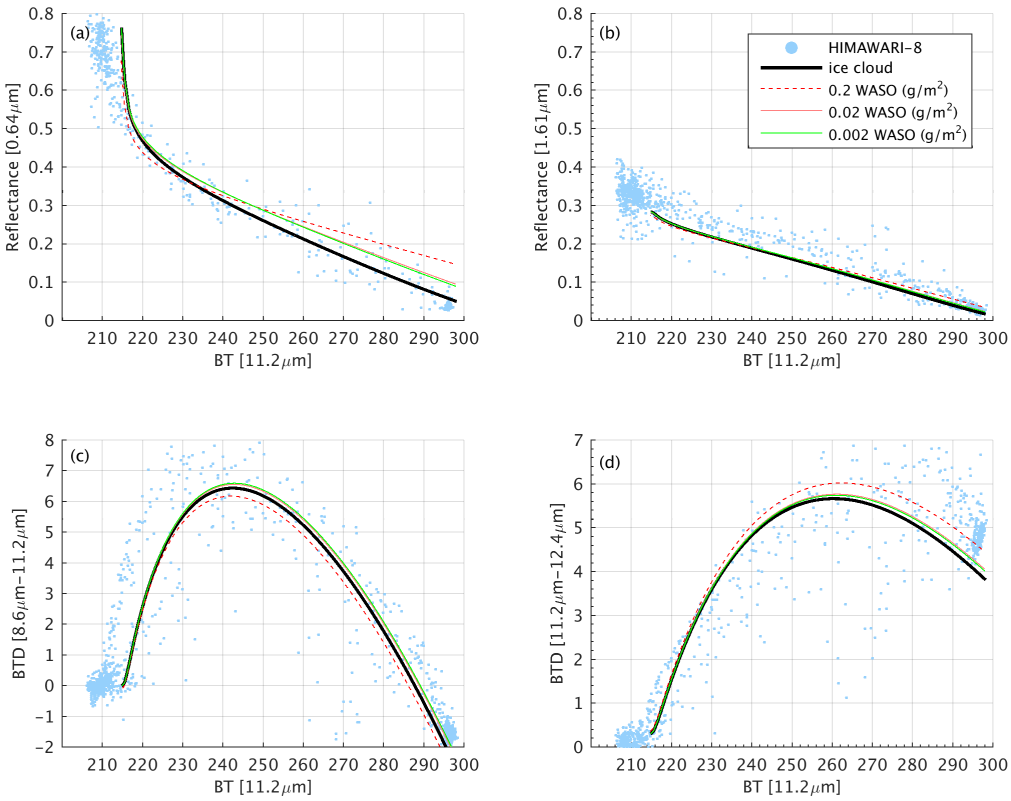

Figure 12. Radiative transfer model results for an ice cloud and aerosol total mass concentration of 0.2, 0.02, and 0.002 g/m^2 above an ice cloud with HYDRA data superimposed (a) the reflectance at 0.64 µm versus the 11.2 µm brightness temperature, (b) the reflectance at 1.61 µm versus the 11.2 µm brightness temperature, (c) BTD (8.6 µm-11.2µm) versus the 11.2 µm brightness temperature, and (d) BTD (11.2 µm-12.4 µm) versus the 11.2 µm brightness temperature.

5. Meteorological Analysis

Since 2013, the Cooperative Institute for Meteorological Satellite Studies (CIMSS) at the University of Wisconsin-Madison has hosted a blog to annotate pyroCb events globally. Since then, over 100 pyroCb events have been documented with satellite imager and other ancillary data. The pyroCb events were first documented using a Yahoo group. Pyroconvection was first detected using satellite imagery, if a fire with pyroconvection produced a cloud formation colder than -40 Celsius at the 11 μm brightness temperature, it was considered a pyroCb event. The pyroCb event would be emailed to all involved in the group, and I would further investigate the pyroCb event using either GOES-15 or HIMAWARI-8.

The satellite imagery was displayed using McIDAS-X, and the images at each time step were used to create a satellite imagery loop. This was useful to see the progression of a pyroCb event. The satellite that I used depended on the location of pyroCb. These pyroCb events occurred in the western United States and Canada, Russia, and Australia. The number of pyroCb cases depended on the year, with the most occurring in 2015. In 2014 there were 52 pyroCb events, in 2015 there were 61, and in 2016 there were 27 cases. We are not entirely sure why there were less pyroCb cases in 2016. We know that 2015 was a very dry year and could be a possible reason for more pyroCb cases this year.

I would collect all the data and add this to my pyroCb database. My database included all the pyroCb events and non-pyroCb events from 2014-2016. A non-pyroCb event is a considered to be a fire or a fire that produced pyroconvection. Pyroconvection (pyroCu)

is different from a pyroCb event because pyroCu does not have minimum brightness temperature threshold. Once a case was documented (pyroCb or non-pyroCb), I investigated the meteorological conditions associated with the event. I used the University of Wyoming website to find sounding profiles that contain meteorological conditions such as Convective Available Potential Energy, RH, dewpoint temperature, temperature, CIN, surface wind, and geopotential height. The purpose of these values are explained further in the following sections. To supplement the radiosonde data, GFS data was also used to analyze the atmosphere above a pyroCb. Variables such as convergence, temperature, geopotential height, RH, and dewpoint temperature were investigated with GFS data.

The meteorological conditions that were investigated were mainly drawn from Peterson et al. 2015. This paper suggested that conditions like upper level convergence, a high Haines Index, low upper tropospheric lapse rate, and moist mid-levels may lead to development of pyroCb. The Haines Index (explained further in section 5.4) measures the ability for a fire to grow. The Haines Index is defined by a number 2-6, the larger the number the more availability for the fire to grow.

The Peterson et al. 2015 paper mainly focused on the Rim Fire and the two pyroCb events that occurred with this fire. With this paper as a basis, I explored further into these meteorological conditions by looking at more than 300 pyroCb and non-pyroCb cases. These meteorological conditions were analyzed using the Heidke Skill Score. The Heidke Skill Score (HSS) is used to determine the skill of a forecast based on the forecast and observations (Barnston 1992). The HSS is a number between negative one (-1) and positive one (+1). If the HSS was closer to positive one (+1) the forecast had more skill (Petty and Li 2013).

In this research, the Heidke Skill Score was used to determine which meteorological conditions were conducive to a pyroCb event. The HSS was calculated for 185 pyroCb cases and 348 non-pyroCb cases. PyroCb cases were drawn from various places across the globe, while non-pyroCb cases were only found in the United States. The resulting Heidke skill scores (not shown) were very small and even negative in some cases. To try to improve the skill score only cases in the western continental United States and Alaska were considered. By limiting the geographic area this reduced the number of pyroCb cases to 41 and the number of non-pyroCb to 315.

The following sections explain each meteorological condition in detail including the threshold used to compute the Heidke Skill Score. Additionally, results of the Heidke Skill Score for each meteorological conditions are found below.

5.1 Convective Available Potential Energy, Convective Inhibition, and Surface Wind

Convective Available Potential Energy (CAPE) was used to estimate the buoyancy available to produce convection in a dry thunderstorm and high altitude smoke plumes (Peterson et al. 2015). Since Peterson et al. 2015 characterize pyroCb's as high-based dry thunderstorms, CAPE was a logical meteorological feature to analyze. CAPE is the measure of instability in the atmosphere and measures the vertical velocity for a thunderstorm (Doswell III and Schultz 2006). The equation for CAPE is:

$$CAPE = R_d \int_{LFC}^{EL} [T'(p) - T(p)] d\ lnp \qquad (19)$$

where R_d is the dry air gas constant, EL equilibrium level, LFC is the level of free convection, p is pressure, $T'(p)$ is the temperature of an air parcel at a pressure level, and $T(p)$ is temperature of the air around the parcel at a pressure level (Petty 2008).

When the CAPE value is large there is a higher updraft velocity (Doswell III and Schultz 2006). However, Fromm et al. (2010) proved that the amount of CAPE varies in pyroCbs with some having little to no CAPE. The one caveat to this conclusion is they investigated only a few pyroCbs. Throughout my research CAPE was investigated for every pyroCb and non-pyroCb case. Without analyzing using the Heidke Skill Score, it was found that CAPE varied with every pyroCb event. Most pyroCb events had little to no CAPE, and some non-pyroCb events had very large CAPE.

Additionally, CAPE values were taken from the radiosonde sounding profile. These determined CAPE values were unreliable because the sounding profiles varied in time, distance, and altitude from the actual location of the pyroCb or non-pyroCb event. Since CAPE was only calculated by the sounding profile it was determined to not be an effective meteorological feature to investigate with respect to pyroCb events. Additionally, a majority of the CAPE values were zero, which contradicts the thought that a pyroCb event would form. CAPE values would have been more reliable closer to the time and location of the pyroCb event.

In addition to CAPE, convective inhibition was also investigated to analyze the buoyancy associated with a pyroCb event. Convective inhibition (CIN) is the amount of energy needed for a parcel to reach its level of free convection (LFC, Petty 2008). If the is CIN value is large it is less likely that external forcing will be enough to initiate convection

(Petty 2008). This thought is there would have to be a low CIN value to aid convection in a pyroCb event. CIN is calculated by the following equation:

$$CIN = R_d \int_{p_o}^{LFC} [T'(p) - T(p)] d\ lnp \quad (20)$$

where the constants are the same as in the CAPE equation, with p_o equal to the surface pressure.

CIN was not evaluated using the Heidke Skill Score because the CAPE was not evaluated using the HSS. However, the average for both pyroCb and non-pyroCb cases were taken from radiosonde sounding profile near the date, time, and location of the case. The purpose of this was to see if there was difference in the mean CIN value between pyroCb and non-pyroCb cases. The hope was to find a major difference in CIN between the two types of cases. However, it was found that the mean value of CIN for pyroCb cases was -88 and for non-pyroCb was -80. A negative CIN value is essential for convection, but there were negative CIN mean values for both pyroCb and non-pyroCb cases. This indicates that CIN is not different from the two types of cases, and would not be a good condition to investigate when trying to deceiver between pyroCb and non-pyroCb cases.

In addition to CAPE and CIN, surface wind was investigated. Surface wind was explored because the thought was if there was large surface wind it would be difficult for a pyroCb to form. Surface wind was not investigated using the Heidke Skill Score, but the mean between the two types of cases was taken. It was found that pyroCb cases had a mean wind of 6.5 knots, and non-pyroCb cases had a mean wind of 7.5 knots. The surface wind for pyroCb cases is less than the surface wind for non-pyroCb cases. This supports the

theory that pyroCb cases need a smaller wind. However, there is not a significant difference between the mean winds in pyroCb versus non-pyroCb cases. This small difference makes it harder to determine how much surface wind is needed for a pyroCb event.

5.2 Relative Humidity

Water vapor enhances the amount of smoke transport beyond the tropopause level (Trentmann et al. 2006). Furthermore, water vapor concentration is greatest right above a fire due to the mixing of the smoke plume with the environment and then decreases with height (Trentmann et al. 2006). Relative humidity is the ratio of partial pressure of water vapor to the vapor pressure of water at a given temperature. This is expressed by the equation:

$$RH = \frac{e}{e_s(T)} \qquad (21)$$

where e is the actual vapor pressure and e_s is the saturation vapor pressure (Petty 2008). RH is important to prove how much water vapor is in the atmosphere. Peterson et al. (2015) showed pyroCbs have conditions favorable to high-base thunderstorms, suggesting high amounts of midlevel moisture. In their analysis of the Rim Fire pyroCb, there was a 60% relative humidity in the 450-650 hPa layer.

For the purposes of this study, I set the threshold of RH to be 50%. Figure 13 displays a pyroCb in British Columbia with contours of RH percentage. For this specific pyroCb the RH is close to 59%. This would be above the 50% threshold, and would agree with the idea that a pyroCb would have formed here.

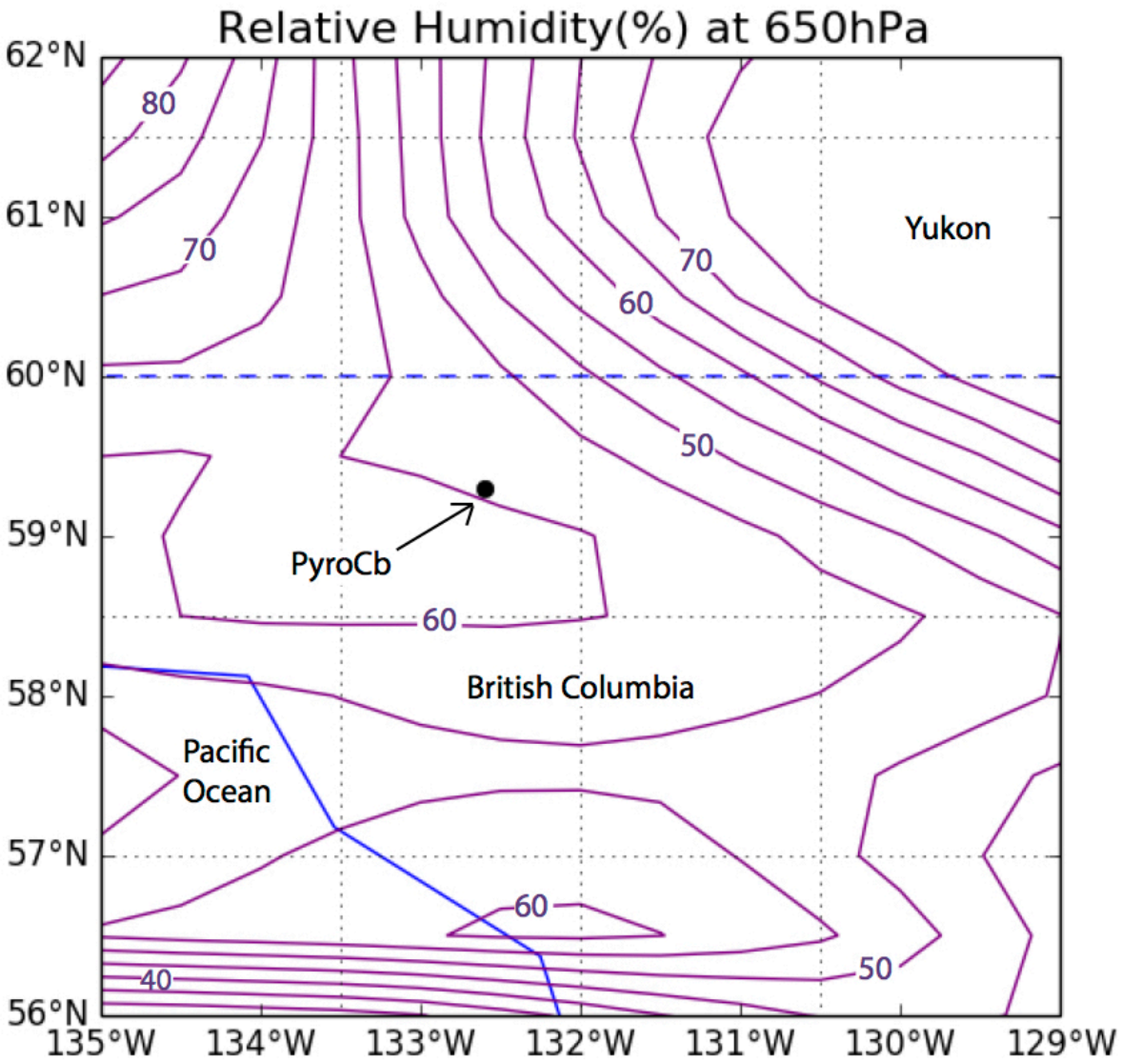

Figure 13. Example of relative humidity contours for pyroCb in British Columbia on 25 May 2015. The pyroCb is indicated by a black dot.

5.3 Convergence

From the previous understanding that pyroCbs are like dry thunderstorms there must be upward vertical motion producing these pyroCbs (Peterson et al. 2015). Convergence at 250 hPa defines vertical motions associated with curved and straight jet (Nauslar et al. 2013). Convergence is defined by the equation:

$$\frac{\partial u}{\partial x} + \frac{\partial v}{\partial y} = -\frac{\partial \omega}{\partial p} \qquad (22)$$

where u, v, and ω are winds in the zonal, meridional, and vertical direction, x and y are zonal and meridional directions, and p is pressure (Gill 1982). In the Peterson et al. (2015) paper they found that negative convergence values were found over the pyroCb events.

Figure 14 is an example of the plotted convergence values near a pyroCb. This figure shows the same pyroCb in British Columbia that was previously plotted. Figure 14 shows the mean sea level pressure at 250 hPa contoured in black, and the convergence values in colored fill. From this example, the convergence value at 250 hPa above the pyroCb is -$9*10^{-5}$ s^{-1}, this coincides with the previous assumption that there is negative convergence above a pyroCb event.

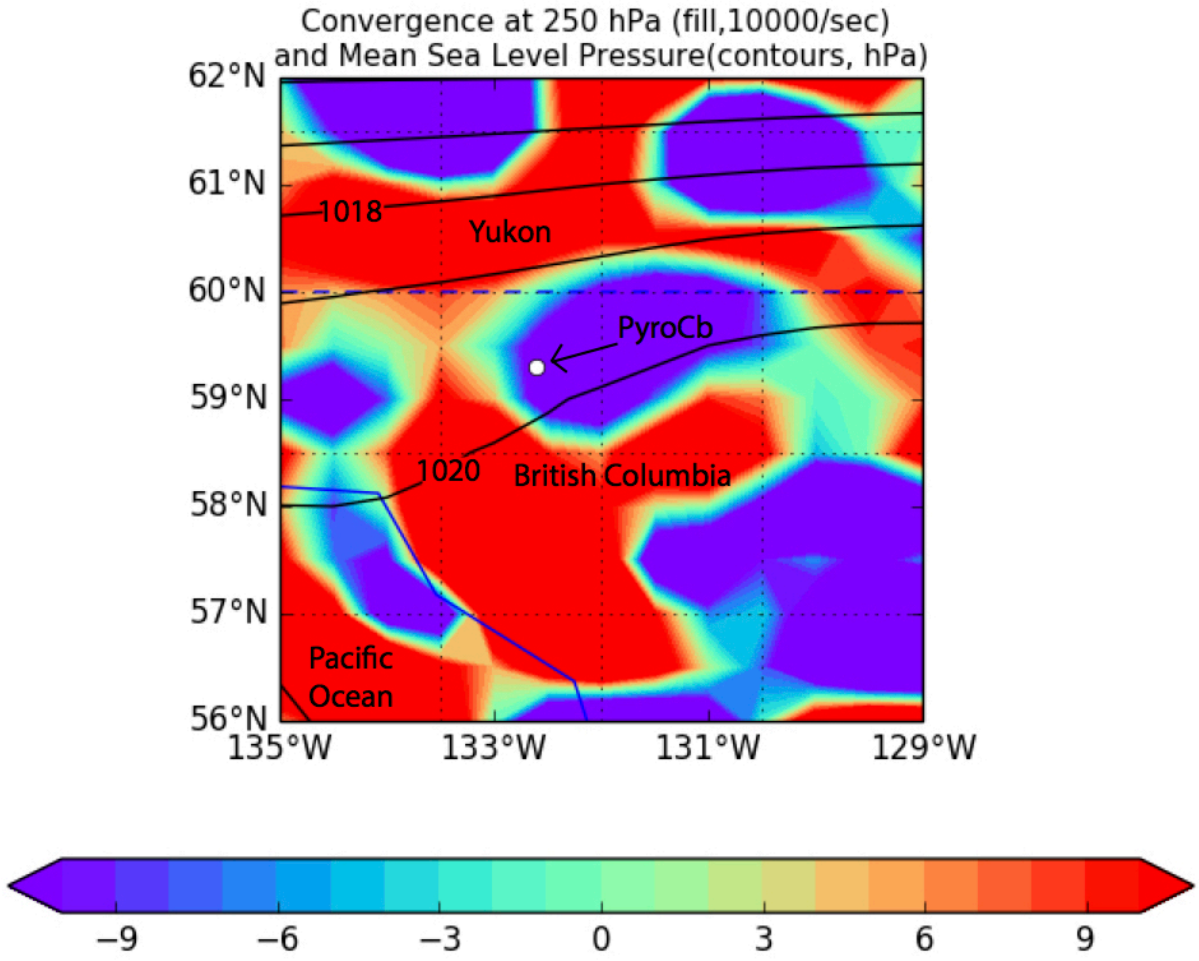

Figure 14. Example of convergence plotted for pyroCb in British Columbia on 25 May 2015. The pyroCb event is indicated by a white dot.

5.4 Haines Index

The Haines Index measures the potential for a wildfire to grow by measuring the dryness and stability over a wildfire (Haines 1988). The Haines Index is essential for fire weather forecasts because it is one of the few above-ground parameters (Potter et al. 2008). This index was initially used to measure the likelihood of a plume-dominated fire to become large or display erratic behavior. This was investigated in this research to better quantify the magnitude of the fire that was being investigated. The Haines Index was measured on a scale from 1-6 based on two equally weighted functions of moisture and stability. The Haines Index can be calculated from mid to low levels, for this research the mid-level Haines Index was calculated, this was between the levels of 850 and 700 hPa. The stability term (A) is defined as:

$$Stability\ difference = T_{850} - T_{700} \quad (23)$$

where T_{850} is the temperature 850 hPa, and T_{700} is the temperature at 700 hPa. The moisture term (B) is defined as:

$$Moisture\ difference = T_{850} - T_{d,850} \quad (24)$$

where T_{850} is the same as above and $T_{d,850}$ is the dewpoint temperature 850 hPa (Potter et al. 2008). The stability and moisture term are given a number 1-3 depending on the stability or moisture difference. Table 3 displays the value of the stability or moisture term for a given difference.

Table 3: Calculating the Haines Index

Stability Term (A)	Moisture Term (B)
A=1 if stability difference is <6^{o}C	B=1 if moisture difference is <6^{o}C
A=2 if stability difference is 6-10^{o}C	B=2 if moisture difference is 6-12^{o}C
A=3 if stability difference is ≥11^{o}C	B=3 if moisture difference is ≥13^{o}C

Both the stability and moisture term were added together to give the Haines Index, a value 2-6. The larger the Haines Index the higher potential for the fire to grow larger and become more erratic (Haines 1988).

Peterson et. al 2015 showed that in their specific cases that a high Haines Index (5 or 6) was ideal for the development of dry thunderstorms and the production of pyroCb events. For this study, we focused on Haines Indices of 4 or greater. This threshold was set to hopefully distinguish the Haines Index between pyroCb and non-pyroCb events.

5.5 Upper Tropospheric Lapse Rate

In Peterson et al. 2015, they found that during a pyroCb event an elevated moist layer must also be conditionally unstable (Peterson et al. 2015). They stated for this to occur the upper tropospheric lapse rate must be less than -7.5^{o}Ckm^{-1}. The upper tropospheric lapse rate (UTLR) was stated to be between 500-300 hPa. The lapse rate is determined by the ratio of the change in temperature over the change in height and is given by the equation:

$$\Gamma = -\frac{\Delta T}{\Delta z} \qquad (25)$$

(Petty 2008). In this equation, ΔT is the change in temperature between 300 and 500 hPa, and Δz is the change in height between these levels.

Peterson et al. (2015) found that in the case of the 2013 Rim Fire the upper-tropospheric lapse rate (500-300 hPa) was less than -7.5^{o}Ckm^{-1}. They argue a steeper UTLR

was favorable to rising motion and may have played a key role in pyroCb formation. To investigate this argument, we looked for a lapse rate of less than -7.5^{o}Ckm^{-1} for a pyroCb event, and a lapse rate greater than this value for a non-pyroCb event.

5.6 Heidke Skill Score

The Heidke skill score was used to characterize the skill of a forecast based on categorical matches between forecasts and observations (Barnston 1992). To differentiate between observed and forecasted events four different letters were used. Table 4 shows the letters associated with each result from the Heidke skill score. For instance, if an event was observed and it was forecasted it would receive the letter "A" and so on.

Table 4: Heidke Skill Score

Event Forecasted	Event Observed	
	Yes	No
Yes	A	B
No	C	D

The Heidke skill score (HSS) was used to determine if a particular threshold for a meteorological condition could predict if a pyroCb or a non-pyroCb event would occur. The forecast in this case were the conditions conducive to pyroCb formation and the observation would be the data collected from GFS or sounding profile data. Once all the cases were collected, each case was assigned appropriate letters. Then the letters are counted for each meteorological condition, and the Heidke skill score was calculated using this equation:

$$HSS = \frac{2(AD-BC)}{[(A+C)(C+D)+(A+B)(B+D)]} \qquad (26)$$

(Petty and Li 2013). If the HSS yielded a score of positive one (+1) this means it had a perfect skill, and a skill score of negative one (-1) meant a perfect negative skill (Petty and Li 2013). For this study we were looking for HSS close to positive one (+1). The Heidke skill score was a useful measure of how well these meteorological conditions were conducive to pyroCb generation.

5.7 Results

The Heidke Skill Score was used to determine if a threshold for a given meteorological condition could differentiate between a pyroCb and non-pyroCb event. Each meteorological condition was given a threshold to predict whether a pyroCb event would occur. For each meteorological condition both pyroCb and non-pyroCb events were used to calculate the Heidke Skill Score. The results are shown in a contingency table that compares predictions with observations for all cases for a given meteorological condition.

5.7.1 Heidke Skill Score Results

The Heidke skill scores for the pyroCb and non-pyroCb cases are found in Table 5. The initial thresholds for each conditions were explained previously in sections 5.2 through 5.5. The resulting Heidke skill scores were relatively low. The perfect skill score would be a value of positive one (+1), but none of the conditions even come within 10 percent of that value. Fortunately, only one condition produced a negative skill score (GFS relative humidity). The rest of the conditions produced a positive skill score, with the highest HSS produced by the sounding UTLR.

Two other high HSSs calculated were GFS UTLR and sounding RH. It can be deduced that the UTLR may be a good meteorological condition to look at in pyroCbs. Both the sounding and GFS data provided a large positive HSS. However, with no meteorological condition coming close to the positive one (+1) HSS goal, these results were inconclusive. Future work into this topic would be investigation into other meteorological conditions and more pyroCb cases.

Table 5: **Calculated Heidke Skill Score**

Data Used	**Heidke Skill Score**
GFS Convergence (0 or less)	0.0234
GFS relative humidity (50% or greater)	-0.0038
GFS Haines Index (4 or greater)	0.0067
GFS Lapse Rate (-7.5^{o}Ckm^{-1} or less)	0.0508
Sounding Relative Humidity (50% or greater)	0.0277
Sounding Haines Index (4 or greater)	0.0178
Sounding Lapse Rate (-7.5^{o}Ckm^{-1} or less)	0.0608

5.7.2 Modified Thresholds

The thresholds for the meteorological conditions from the previous Heidke skill score were taken from Peterson et al. 2015 paper and were found to be inconclusive. The thresholds were then modified in hopes to improve the HSS. Figures 15-18 show the different thresholds and the resulting HSS for a given meteorological condition.

Figure 15 shows the HSS for different thresholds of convergence. From this plot it is evident that the greatest HSS is when the threshold for convergence is 0. Additionally, once the threshold decreases so does the HSS. The HSS proves that for a larger value of convergence the HSS is greater. With a negative skill score for negative convergence values, this is opposite of the initial theory that negative convergence values are need for a pyroCb event.

The next meteorological condition investigated was relative humidity. Figure 16 shows the HSS versus different relative humidity percentages for both GFS and sounding data. One notable difference between the two data sources is the GFS HSS does not vary much between different relative humidity values. The resulting HSS is close to zero for all the relative humidity values proving there is no difference between the relative humidity values from pyroCb and non-pyroCb cases. The sounding data's HSS varied more with the greatest HSS around 40%. This suggest that pyroCb events only need around 40% relative humidity to form, which is less than the 60% previously thought.

In addition, the different thresholds of the Haines Index were investigated. Figure 17 shows the calculated HSS versus the Haines Index for both GFS and sounding data. The HSS for both data sources are very small and near zero. This suggests that the Haines Index values are the same in both pyroCb and non-pyroCb cases. The Haines Index determines the ability for a fire to grow, so it is logical that the Haines Index would be large for pyroCb and non-pyroCb events. In conclusion, the findings here indicate that the Haines Index would not be a meteorological condition to look at when determining if a fire will become a pyroCb event.

The last meteorological condition investigated with the HSS was the UTLR. The HSS results with varying thresholds of UTLR are found in Figure 17. For the most part the HSS for all UTLR are positive, which suggests a positive skill for this condition. The largest HSS for both data sources was around -8^{o}C/km. This is steeper than the UTLR of -7.5 ^{o}C/km suggested in Peterson et al. 2015. With the steeper UTLR we are able to separate the pyroCb events from the non-pyroCb events more efficiently. The large HSS found for the UTLR suggests that the UTLR may be a condition conducive to pyroCb events.

In conclusion, changing the thresholds for each meteorological condition provided information on which threshold produced the best HSS. Once the thersholds were modified the Heidke Skill Scores did not improve, and the results are still inconclusive. However, the HSS provided insight into which meteorological conditions were more useful when looking at pyroCb events (i.e. upper tropospheric lapse rate) . The research can be expanded to more meteorological conditions and pyroCb events in hopes of find the condition that occurs in all pyroCb events.

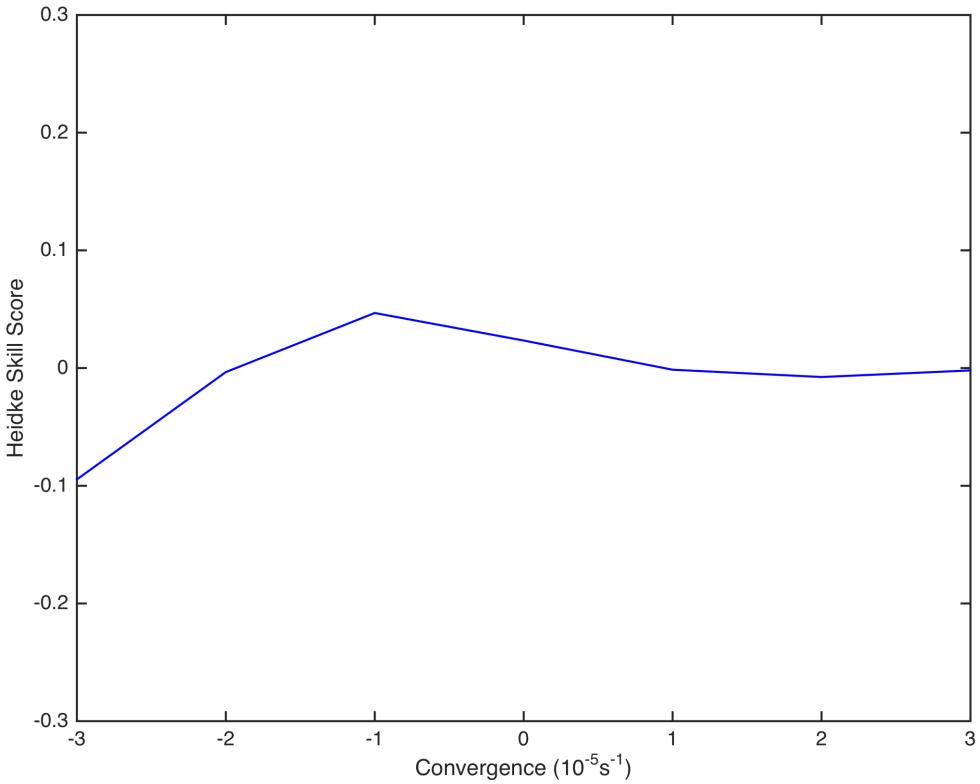

Figure 15. Heidke Skill Score versus different thresholds of convergence ($10^{-5}s^{-1}$).

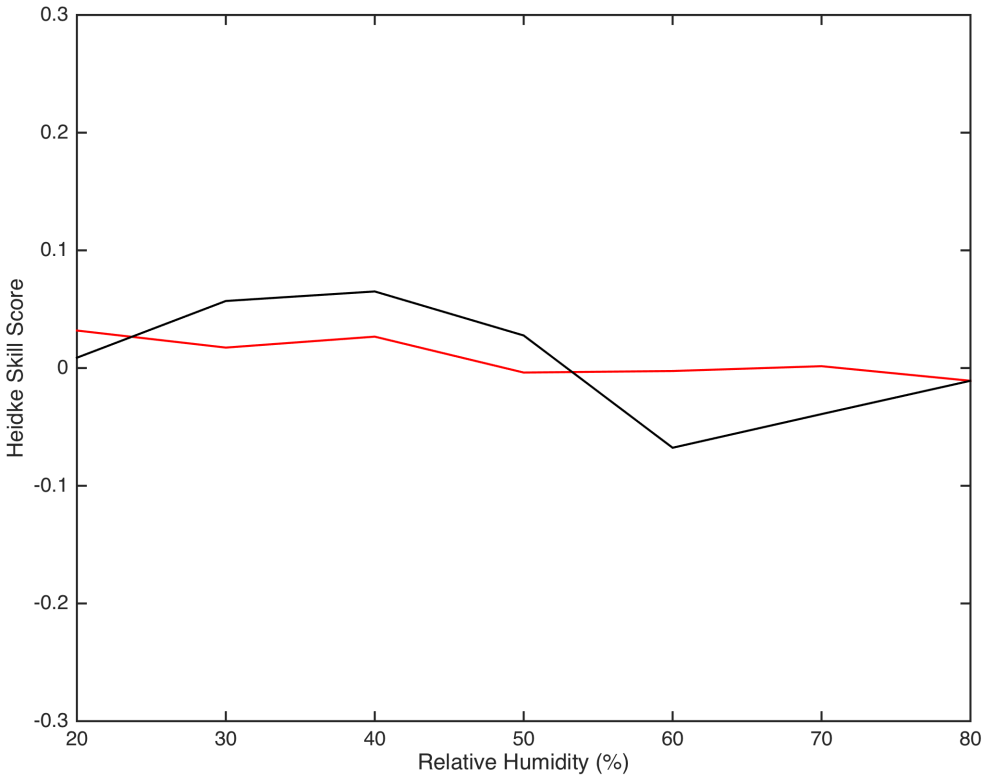

Figure 16. Heidke Skill Score versus different thresholds of relative humidity (%). The red line represents GFS data and the black line represents sounding data.

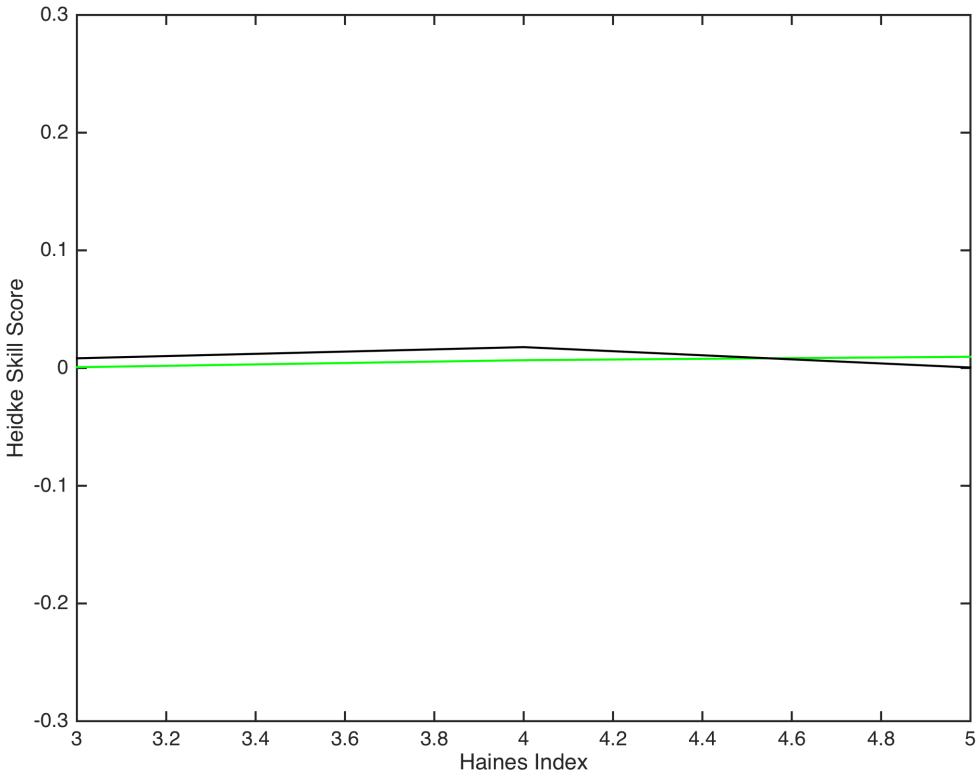

Figure 17. Heidke Skill Score versus different thresholds of the Haines Index. The green line represents GFS data, and the black line represents sounding data.

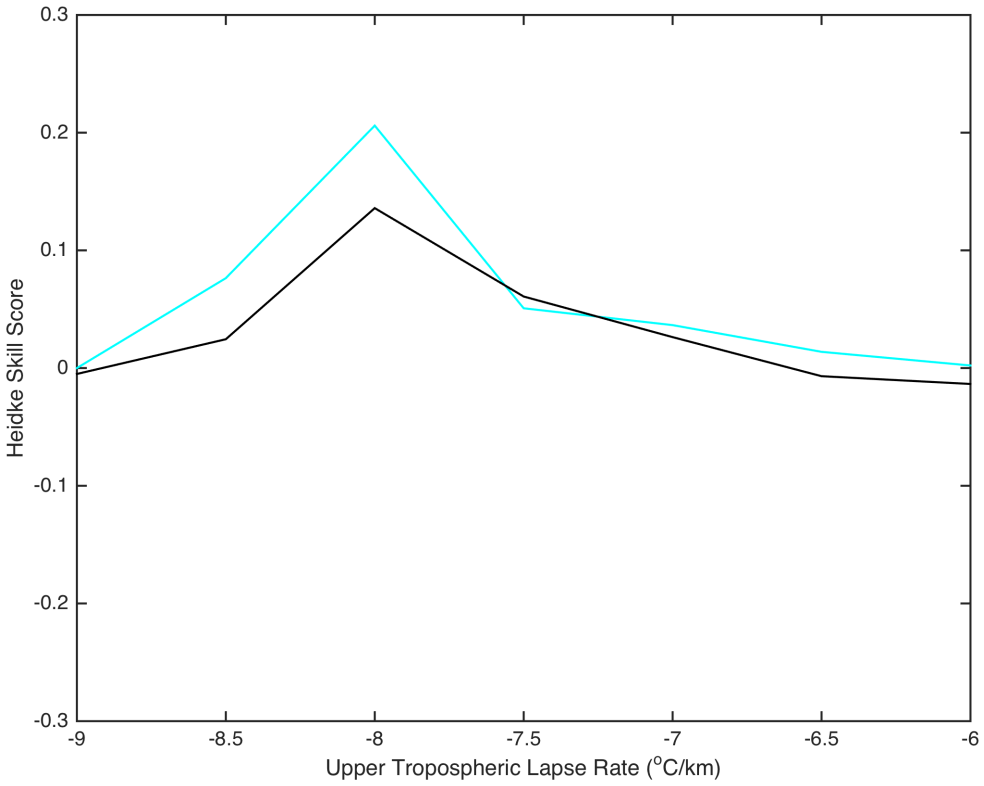

Figure 18. Heidke Skill Score versus Upper Tropospheric Lapse Rate (^{o}C/km). The cyan line represents GFS data, and the black line represents sounding data.

6. Conclusions

PyroCb events are fire started cumulus clouds whose structure reflects that of a dry thunderstorm. These pyroCb events can inject large amounts of smoke into the UT/LS, thus impacting reflectance and brightness temperature retrievals. The theory was with the presence of smoke the reflectance and brightness temperature would decrease. This research had two overarching goals. The first explored the radiative transfer equation for both a pristine ice cloud and a smoke layer above an ice cloud. The second goal investigated the meteorological conditions conducive to a pyroCb event. The meteorological conditions were suggested in the Peterson et al. 2015 and included Haines Index, convergence, upper tropospheric lapse rate, and relative humidity. These conditions were assessed using a Heidke Skill Score that determined whether the condition was conducive to a pyroCb event.

A radiative transfer model was used to investigate the impact of a pyroCb event on the interpretation of satellite imagery. The model outputs were compared to satellite data from a pyroCb event in hopes of finding similarities. A radiative transfer model was calculated using libRadtran for a pristine ice cloud, and for a smoke layer above an ice cloud. Water-soluble aerosols were used as the smoke layer; these aerosols mimic the composition of a biomass-burning event. The model's output consisted of radiances values for both solar and thermal wavelengths that were converted to reflectance and brightness temperature values. The model outputs for the two scenarios were then compared to HIMAWARI-8 data of a pyroCb event in Australia on 06 December 2016. The model output matched the satellite data better for a pristine ice cloud compared to a smoke layer. Overall, the comparisons showed it is hard to match model output to satellite data.

However, the model did provide data on the height of the ice cloud and smoke layer, and the thickness of the smoke layer.

The second goal was investigating meteorological conditions conducive to a pyroCb event. The meteorological condition data were extracted from GFS and radiosonde sounding profiles. Roughly 40 pyroCb cases and around 300 non-pyroCb cases in the western United States and Alaska were analyzed using a Heidke skill score. The Heidke Skill Score determined the amount of skill a meteorological condition had based on forecast and observational data. If the Heidke Skill Score for a given meteorological condition was close to positive one (+1) this indicated that a pyroCb was forecasted to happen and observationally it did. The resulting Heidke Skill Score gave an indication if the meteorological condition occurred in every pyroCb event. The goal was to find a meteorological condition that could be used to determine if a pyroCb event would form from a fire. Unfortunately, the results from the Heidke Skill Score were near zero and inconclusive, with no meteorological condition occurring at every pyroCb. However, further research can be done into new meteorological conditions and more pyroCb events in hopes of finding a meteorological condition that can determine if a pyroCb event will form.

7. References

Akpootu, D. O. and M. Momoh: The scattering coefficient, extinction coefficient, and single scattering albedo of water soluble in the radiative forcing of urban aerosols. *Arch. Appl. Sci. Res.,* **5(2),** 109-120, 2013.

Al-Saadi J, Soja A, Pierce B, Kittaka C, Emmons L, Kondragunta S, Zhang X, Wiedinmy C, Schaack T, Szykman J: **Global Near-Real-Time Estimates of Biomass Burning Emissions using Satellite Active Fire Detections**. *Presented at 16th International Emission Inventory Conference, Raleigh, NC, May 14-17, 2007*[http://www.epa.gov/ttn/chief/conference/ei16/].

Barnston, Anthony G. :Correspondence among the Correlation, RMSE, and Heidke Forecast Verification Measures; Refinement of the Heidke Score. *Wea. Forecasting Weather and Forecasting* 7.4 (1992): 699-709.

Baum, Bryan A., D. P. Kratz, P. Yang, S.C. Ou, Y. Hu, P.F. Soulen, and Si-Chee Tsay: Remote sensing of cloud properties using MODIS airborne simulator imagery during SUCCESS 1. Data and models. *Journal of Geophysical Research,* **105**,11767-11780, 2000.

— , P.F. Soulen, K. I. Strabala, M. D. King, S. A. Ackerman, W. P. Menzel, and P. Yang: Remote sensing of cloud properties using MODIS Airborne Simulator imagery during SUCCESS. II. Cloud thermodyhanmic phase. *J. Geophys. Res*., **105**, 11,781 11,792, 2000b.

— , P. Yang, A. J. Heymsfield, S. Platnick, M. D. King, Y. X., Hu, and S. T. Bedka: Bulk Scattering Properties for the Remote Sensing of Ice Clouds. Part II: Narrowband Models. *Journal of Applied Meteorology,* **44**, 1896-1911, 2005.

— , P. Yang, A. J. Heymsfield, A. Bansemer, A. Merrelli, C. Schmitt, and C. Wang, 2014: Ice cloud bulk single-scattering property models with the full phase matrix at wavelengths from 0.2 to 100 µm. *J. Quant.,* **146**, 123-129, 2014, doi: 10.1016/j.jqsrt.2014.02.029

British Crown. "A Library Providing Cartographic Tools for Python." *Cartopy Homepage*. Met Office, 2015. Web. 10 Aug. 2016.

Chandrasekhar, S.: Radiative Transfer. *Dover,* 1960.

Chylek, P. and J. Wong: Effect of absorbing aerosols on global radiation budget. *Geophysical Research Letters,* **22(8)**, 929-931, 1995.

Dalzell, W. H. and A. F. Sarofim: Optical Constraints of Soot and Their Application to Heat Flux Calculations. *J. Heat Transfer*, **91(1)**, 100-104, 1969.

Damoah, R., N. Spichtinger, R. Servranckx, M. Fromm, E. W. Eloranta, I. A. Razenkov, P. James, M. Shulski, C. Forster, and A. Stohl: A case study of pyro-convection using transport model and remote sensing data. *Atm. Chem and Phys.,* **6**, 173-185, 2006.

Dawson, Andrew. *Windspharm: Spherical Harmonic Wind Analysis in Python*. N.p., 2012. Web. 10 Aug. 2016.

Doswell III, C. A. and D. M. Schultz: On the Use of Indices and Parameters in Forecasting Severe Storms. *EJSSM*, **1(3)**, 2006.

Freitas, S. R., K. M. Longo, R. Chatfield, D. Latham, M. A. F. Silva Dias, M. O. Andreae, and J.A. Carvalho Jr.: Including the sub-grid scale plume rise of vegetation fire in low resolution atmospheric transport models. *Atms. Chem. Phys.*, **7**, 3385-3398, doi:10.1029/2005GL025161, 2006.

Fromm, M. D., D. T. Lindsey, R. Servranckx, G. Yue, T. Trickl, R. Sica, P. Doucet, and S. Godin Beekmann: The untold story of pyrocumulonimbus. *Bull. Amer. Meteor. Soc.,* **91,** 1193–1209, doi:10.1175/2010BAMS3004.1, 2010.

— , J. Alfred, K. Hoppel, J. Hornstein, R. Bevilacqua, E. Shettle, R. Servranckx, Z. Li, and B. Stocks: Observations of boreal forest fire smoke in the stratosphere by POAM III, SAGE II, and lidar in 1998. *Geophysical Research Letters,* **27(9),** 1407-1410, 2000.

— , R. Bevilacqua, R. Servranckx, J. Rosen, J. Thayer, J. Herman, and D. Larko: Pyro cumulonimbus injection of smoke to the stratosphere: Observations and impact of a super blowup in northwestern Canada on 3-4 August 1998. *Jour. Of Geo. Res.,* **110,** doi:10.1029/2004JD00530, 2005.

— , R. H. D. McRae, J. J. Sharples, and G. P. Kablick III: Pyrocumulonimbus pair in Wollemi and Blue Mountains National Parks, 22 November 2006. *Aust. Meteor. Oceanogr. J.,* **62,** 117–126, 2012.

— , and R. Servanckx : Transport of forest fire smoke above the tropopause by supercell convection, Geophs. Res., Lett., **30**, 1542, doi:10.1029/2002GL016820, 2003.

Gatebe, C.K., T. Varnai, R. Poudyal, C. Ichoku, and M. D. King: Taking the Pulse of PyroCumulus Clouds. *Atmospheric Environment,* **52**, doi: 10.1016/j.atmosenv.2012.01.045, 2012.

Gill, A. E.: Atmosphere-Ocean Dynamics, Academic Press, 1982.

Goose, S., D. Labrie, and P. Chylek: Refractive index of ice in the 1.4-7.8 µm spectral range, *Appl. Opt*., *34*, 6582-6586, 1995.

Guan, H., R. Esswein, J. Lopez, R. Bergstrom, A. Warnock, M. Follette-Cook, M. Fromm, and L. T. Iraci: A multi-decadal history of biomass burning plume heights identified using aerosol index measurements. *Atm. Chem. And Phys.*, **10**, 6461-6469, doi:10.5194/acp-10-6461-2010, 2010.

Haines, D. A.: A lower atmospheric severity index for wildland fire. *Natl. Wea. Dig.*, **13**, 23–27, 1988.

Hansen, J. E., and L. D. Travis: Light scattering in planetary atmospheres, *Space Sci. Rev.,* **16***,* 527-610, 1974.

Hess, M., P. Koepke, and I. Schult: Optical Properties of Aerosols and Clouds: The Software Package OPAC. *Amer. Met. Soci.,* **79**, 831-844, 1998.

Hillger, Donald W. and T. J. Schmit, 2011: The GOES-15 Science Test: Imager and Sounder Radiance and Product Validations. Accessed 02 April 2016. [Available online at http://rammb.cira.colostate.edu/projects/goesp/NOAA_Technical_Report_141_GOES-15_Science_Test.pdf]

Hunter, John, Daren Dale, Eric Firing, Michael Droettboom, and Matpotlib Development Team. "Introduction." *Matplotlib: Python Plotting — Matplotlib 1.5.1 Documentation*. N.p., 2002. Web. 10 Aug. 2016.

Hyvärinen, Otto. "A Probabilistic Derivation of Heidke Skill Score." *Wea. Forecasting Weather and Forecasting,* **29(1)**, 177-81, 2014.

Ichoku, Charles: Satellite Characterization of Biomass Burning and Smoke Emissions in Africa. *Remote Sensing of the Environment*, **112 (6)**, 2950-2962, doi:10.1016/j.rse.2008.02.009, 2008.

IPCC. (2007), Contribution of Working Group I to the Fourth Assessment Report of the Intergovernmental Panel on Climate Change (2007) edited by S. Solomon, D. Qin, M. Manning, Z. Chen, M. Marquis, K. B. Averyt, M. Tignor, and H. L. Miller, Cambridge University Press, Cambridge, UK and New York, NY, USA.

Jacob, Daniel J.: Introduction to Atmospheric Chemistry, Princeton University Press, 1999.

Kopacz, M., D. L. Mauzerall, J. Wang, E. M. Leibensperger, D. K. Henze, and K. Singh: Origin and radiative forcing of black carbon transported to the Himalayas and Tibetan Plateau. *Atmos. Chem. Phys*., **11(6)**, 2837-2852, doi:10.5194/acp-11-2837 2011.

Kuo, H. L.: Further Studies of the Parameterization of the Influence of Cumulus Convection on Large-Scale Flow. *Jour. Atm. Sci.*, **31**, 1232-1240, 1974.

Lareau, Neil P., and Craig B. Clements: "Environmental controls on pyrocumulus and pyrocumulonimbus initiation and development." *Atmos. Chem. Phys.,* **16,** 4005 1022, doi:10.5194/acp-16-4005-2016, 2016.

Lindsey, Daniel T., and Michael Fromm: Evidence of the Cloud Lifetime Effect from Wildfire-induced Thunderstorms. *Geophys. Res. Lett.,* **35(22)**, 2008.

Luderer, G., J. Trentmann, T. Winterrath, C. Textor, M. Herzog, H. F. Graf, and M. O. Andrae: Modeling of biomass smoke injection into the lower stratosphere by a large forest fire (Part II): sensitivity studies. *Atmos. Chem. Phys.*, **6**, 5261-5277, 2006.

— , J. Trenmtann, and M.O. Andreae: A new look at the role of fire-released moisture on the dynamics of atmospheric pyro-convection. *Int. J. Wildland Fire,* **18**, 554-562, doi:10.1071/WF07035, 2009.

Mayer B., and A. Kylling: Technical note: The libRadtran software package for radiative transfer calculations- description and examples. *Amer. Chem. Phys.,* **5**, 1855-1877, 2005.

Nakajima, Teruyuki and Michael D. King: Determination of the Optical Thickness and Effective Particle Radius of Clouds from Reflected Solar Radiation Measurements. Part I: Theory. *Jour. Of the Atm. Sci.*, **47**, 1879-1893, 1990.

Nauslar, N. J., M. L. Kaplan, J. Wallmann, and T. J. Brown: A forecast procedure for dry thunderstorms. *J. Oper. Meteor.,* **1**, 200-214, doi:10.15191/nwajom.2013.0117, 2013.

NCAR. "NCEP Climate Forecast System Version 2 (CFSv2) 6-hourly Products." *Research Data Archive.* 24 July 2017.

Peterson, D. A., E. J. Hyer, J. R. Campbell, M. D. Fromm, J. W. Hair, C. F. Butler, and M. A. Fenn: The 2013 Rim Fire: Implications for Predicting Extreme Fire Spread, Pyroconvection, and Smoke Emissions. *Amer, Meteor. Soc.,* **96***,* 229-247, doi:10.1175/BAMS-D-14-00060.1, 2015.

—, —, and J. Wang. Quantifying the Potential for High-altitude Smoke Injection in the North American Boreal Forest Using the Standard MODIS Fire Products and Subpixel based Methods. *Journal of Geophysical Research: Atmospheres J. Geophys. Res. Atmos.* **119(6),** 3401-419, 2014.

—, M. Fromm, J. Solbrig, E. Hyer, M. Surratt, and J. Campbell: Detection and Inventory of Intense Pyroconvection in Western North American using GOES-15 Daytime Infrared Data. *Journal of Applied Meteorology and Climatology,* **56,** 471-493, doi:10.1175/JAMC-D-16-0226.1, 2017.

—, J. Wang, C. Ichoku, and L. A. Remer: Effects of lightning and other meteorological factors on fire activity in the North American boreal forest: Implications for fire weather forecasting. *Atmos. Chem, Phys*., **10**, 6873-6888, doi:10.5194/acp-10-6873 2010.

Petty G. W.: "A First Course in Atmospheric Radiation". *Sundog Publishing*, 2006.

— : "A First Course in Atmospheric Thermodynamics". *Sundog Publishing*, 2008.

— , K. Li: Improved Passive Microwave Retrievals of Rain Rate over Land and Ocean Part II: Validation and Intercomparison. *Amer. Meteor. Soc*., **30**, 2509-2526, doi:10.1175/JTECH-D-12-00184.1, 2013.

Potter, B. E.: The role of released moisture in the atmospheric dynamics associated with wildland fires. *Int. J. Wildland Fire,* **14**, 77-84, doi:10.1071/WF04045, 2005.

— , Julie A. Winkler, Dwight F. Wilhelm, Ryan P. Shadbolt, and Xindi Bian: Computing the Low-Elevation Variant of the Haines Index for Fire Weather Forecasts. *Amer. Meteor. Soc.,* **23**, 159-167, doi:10.1175/2007/WAF2007025.1.

Pozo D., F.J. Olmo, and L. Alados-Arboleda: Fire detection and growth monitoring using a multitemporal technique on AVHRR mid-infrared and thermal channels.*Remote Sensing of Environment,* **60**, 111-120, doi:10.1016/S0034-4257(96)00117-4, 1997.

Randerson, J.T., H. Liu, M.G. Flanner, S. D. Chambers, Y. Jin, P.G.Hess, G. Pfister, M.C. Mack, K.K. Treseder, L. R. Welp, F. S. Chapin, J. W. Harden, M. L. Goulden, E. Lyons, J. C. Neff, E. A. G. Schuur, C. S. Zender: The impact of boreal forest fire on climate warming. *Science*, **314(5802)**, 1130-1132, doi:10.1126/science.1132075, 2006.

Riehl, H.: On the role of the tropics in the general circulation. *Tellus*, **2**, 1-17, 1950.

— , and J. S. Malkus: Some aspects of hurricane Daisy. *Tellus,* **13**, 181-213, 1961.

Rink, T., W. P. Menzel, P. Antonelli, T. Whittaker, K. Baggett, L. Gumley, and A. Huang: Introducing HYDRA. *Amer. Meteor. Soc.,* **88**, 159–166, doi: 10.1175/BAMS-88-2-159, 2007.

Rosenfeld, D., M. Fromm, J. Trentmann, G. Luderer, M. O. Andreae, and R. Servranckx: The Chisholm firestorm: observed microstructure, precipitation and lightning activity of a pyro-Cb. *Atm. Chem. And Phys.,* **6**, 9877-9906, 2006.

Stamnes, K., S-C. Tsay, W. Wiscombe, and K. Jayaweera: Numerically stable algorithm for discrete-ordinate-method radiative transfer in multiple scattering and emitting layered media. *Applied Optics,* **27(12)**, 2502-2509, 1988.

— , S-C. Tsay, W. Wiscombe, and K. Jayaweera: An Improved, Numerically Stable Computer Code for Discrete-Ordinate-Method Radiative Transfer in Scattering and Emitting Lyaered Media. *NASA Report*, 1988.

— and H. Dale: A New Look at the Discrete Ordinate Method for Radiative Transfer Calculation in Anisotropically Scattering Atmospheres, II: Intensity Computations. *J. Atmos. Sci.*, **38**, 2696, 1981.

— And R. A. Sawnson: A New Look at the Discrete Ordinate Method for Radiative Transfer Calculation in Anisotropically Scattering Atmospheres. *J. Atmos. Sci.*, **38**, 387, 1981.

Stocks, BJ., B.M. Wotton, M.D. Flanningan, M.A. Fosberg, D.R. Cahoon, and J.G. Goldammer: Boreal Forest Fire Regimes and Climate Change, *Wengen-99 Global Change Workshop, September 1999, Wengen, Switzerland,* in press, 2000.

Stone, R. S., G. L. Stephens, C. M. R. Platt, and S. Banks: The remote sensing of thing cirrus cloud using satellites, lidar and radiative transfer theory. *J. Appl. Meteorol.,* **29**, 353-366, 1990.

Suomi V. E., R. Fox, S. S. Limaye, and W. L. Smith: McIDAS III: A Modern Interactive Data Access and Analysis System. *Jour. Of Climate and Appl. Met.,* **22**, 766-778, 1983.

Trentmann, J., G. Luderer, T. Winterrath, M. D. Fromm, R. Servranchx, C. Textor, M. Herzog, H.-F Graf, and M.O. Andreae: Modeling of bio- mass smoke injection into the lower stratosphere by a large forest fire (Part I): Reference simulation. *Atmos. Chem. Phys.,* **6,** 5247–5260, doi:10.5194/acp -6-5247-2006, 2006.

Twomey, S.: The Influence of Pollution on the Shortwave Albedo of Clouds. *Jour. Of the Atm. Sci.,* **34**, 1149-1152, 1977.

Wallmann, J., R. Milne, C. Smallcomb, and M. Mehle: Using the 21 June 2008 California lightning outbreak to improve dry lightning forecast procedures. *Wea. Forecasting*, **25**, 1447-1462, doi: 10.1175/2010WAF2222393.1, 2008

Wang, C: A modeling study of the response of tropical deep convection to the increase of cloud condensation nuclei concentration: 1. Dynamics and microphysics. *J. Geophys. Res.,* **110**, doi:10.1029/2004JD005720, 2005.

Wang, J., S. A. Christopher, U. S. Nair, J. S. Reid, E. M. Prins, J. Szykman, and J. L. Hand: Mesoscale modeling of Centeral American smoke transport to the United States: 1. "Top-down" assessment of emissions strength and diurnal variation impacts. *J. Geophys. Res.,* **11**, D06S17, doi: 10.1029/2005JD006416, 2006.

—, C. Ge, Z. Yang, E. J. Hyer, J. S. Reid, B.-N. Chew, M. Mahmud, Y. Zhang, and M. Zhang: Mesoscale modeling of smoke transport over the Southeast Asian Maritime Continent: Interplay of sea breeze, trade wind, typhoon, and topography. *Atmos. Res.,* **122**, 486-503, doi:10.1016/j.atmosres.2012.05.009, 2013.

Warren, S. G., Optical constants of ice from the ultraviolet to the microwave, *Apple Opt*., *23*, 1206-1224, 1984.

—, and R. E. Brandt: Optical constants of ice from the ultraviolet to the microwave: A revised compilation. *J. Geophys. Res.*, **113**, D14220, doi:10.1029/2007JD009744, 2008.

Wyser, Klaus: The Effective Radius in Ice clouds. *Journal of Climate,* **11**, 1793-1802, 1998.